Host-Dependent Vascularization in Cardiac Tissue Engineering

Eileen Brady

A dissertation

submitted in partial fulfillment of the

requirements for the degree of

Doctor of Philosophy

University of Washington

2021

Reading Committee:

Kelly R Stevens, Chair

Ying Zheng

Nate J Sniadecki

Program Authorized to Offer Degree:

Molecular and Cellular Biology

University of Washington

Abstract

Host-dependent Vascularization in Cardiac Tissue Engineering

Eileen Brady

Chair of the Supervisory Committee:
Kelly R. Stevens PhD, Assistant Professor
Bioengineering

Cardiac tissue engineering could address the growing need for donor hearts by supplying an alternative source of human myocardium. However, vascularization remains a barrier to clinical translation of this technology. While a variety of strategies have been developed to vascularize engineered tissues, it is not known whether these methods can be successfully applied across different host contexts. In this thesis, we use a previously developed method of guiding vascularization with patterned endothelial “cords” to study the integration of artificial tissues across implant locations and species. First, we describe an aberrant host response to guided vascularization in the athymic rat heart. Instead of finding patterned vasculature as has been previously reported, we found loss of patterning and robust inflammation. To investigate the host factors that could explain these results, we next compared the response to artificial patches implanted in different implant sites (IP and heart) and species (mouse and rat). Comparison of responses to artificial tissues between athymic mice and athymic rats revealed host differences in inflammation, cardiomyocyte engraftment, and vascularization. These results demonstrate the critical importance of host biology to the integration of engineered tissues. Future work is needed to understand and optimize specific host factors that control vascularization and tissue engraftment.

TABLE OF CONTENTS

LIST OF FIGURES

ACKNOWLEDGEMENTS

I am grateful for the colleagues, mentors, friends, and family who have supported me throughout this journey. First, I would like to thank my advisor, Prof. Kelly Stevens, who has provided primary scientific and career mentorship. I have benefited from Dr. Stevens’ commitment not only to my academic success, but also her obvious care for my personal development. Additionally, I thank my committee members Prof. Chuck Murry, Prof. Ying Zheng, Prof. Nate Sniadecki, and Prof. Ashleigh Theberge for their advice and support throughout the development of this project. Your insights and suggestions have challenged me to think in creative ways about scientific problems. I would also like to thank the directors and administrators of the Molecular and Cellular Biology graduate program and the Medical Scientist Training program. I deeply appreciate your willingness to answer questions as well as all the behind the scenes work you do to support students.

To all the current and past members of the Stevens lab, especially Chelsea Fortin, Mary Regier, Emily Olszewski, Colleen O’Connor, Sarah Saxton, Fredrik Johansson, and Daniel Corbett, thank you all for being not only wonderful colleagues, but also dear friends. As I have spent the last year of my thesis in the relative isolation of the COVID-19 pandemic, I am more grateful than ever for the virtual and in-person connections I have shared with Stevens’ lab members. A special thank you to Fredrik: without your surgical expertise and calming presence, the work in this thesis could not have been completed.

Beyond the Stevens lab, I would like to thank colleagues and collaborators throughout the Institute for Stem Cell and Regenerative Medicine. I am particularly grateful for the assistance Dale Haley has provided through the Garvey Imaging Core, which was used to generate most of the images in this document. Additionally, special thanks to members of the Jennifer Davis' lab, especially Amy Martinson, who was generous with her time and talents as we moved to implant cardiac patches in mice.

Last, I would like to acknowledge the support I have received from my family and friends who have been there for me both in time of celebration as well as times of challenge. I could not have gotten to where I am without you all.

CHAPTER 1. INTRODUCTION

1.1 ABSTRACT

The survival of vertebrate organisms depends on highly regulated delivery of oxygen and nutrients through vascular networks that are embedded in nearly all tissues in the body. Dysregulation of these vascular networks is implicated in many of the most common, debilitating, and deadly human diseases such as hypertension, coronary artery disease, diabetes, and cancer. Because of the critical importance of vasculature, engineers have sought to create artificial vascular networks within artificial tissues for organ engineering applications, as well as in model systems for human disease and pharmacologic testing. Despite their importance and potential utility, engineering vascular networks has remained difficult due to both incomplete understanding of vascular biology, as well as technical limitations for vascular fabrication. Recent materials advances have enabled transformative progress in vascular engineering by ushering in a plethora of new tools for both deconstructing and constructing vasculature. Whole tissue imaging[1–4] and single cell spatial ‘omics technologies[5,6] have now put the field within reach of comprehensive, organ-specific atlases of vasculature that could serve as “blueprints” for engineers[7]. New fabrication methods such as bioprinting[8], vascular organoids[9,10], and microfluidic organ-on-chip systems[11] can construct perfusable 3D continuous topologies at a cellular scale. The convergence of these technologies poises the field to overcome historical limitations and opens the door for engineering the multi-scale complexity of vascular networks found in nature. In Chapters One and Two, we explore vascular network development in natural and artificial systems and evaluate progress towards engineering vascular networks. We also define remaining knowledge gaps, highlight critical emerging frontiers, and identify clinical opportunities for this field.

1.2 CLINICAL NEED FOR ENGINEERED VASCULAR NETWORKS

Simple multicellular organisms such as flatworms can supply all their tissues with oxygen via passive diffusion through the body surface[12]. However, as organisms grew in size and complexity, they required new strategies for delivering oxygen and nutrients throughout the body. To meet this demand, vertebrates developed a system of hollow conduits to facilitate fluid transport to distant tissues. The survival of vertebrates depends on these carefully regulated vascular networks to match the delivery of oxygen and nutrients with tissue demand. The critical importance of vascular networks to vertebrate survival motivates the engineering of artificial vasculatures, which would allow deeper insight into basic vascular biology and could address some of the greatest clinical needs in human health.

Engineered vascular networks could meet several clinical needs. First, engineered vasculature could address the growing mismatch between the demand for transplantable human organs and the number of available donor organs. Vascularization would enable the generation of tissues that approximate the thickness found in commonly transplanted human organs such as kidney, liver, heart, and lung, thereby providing an alternative source of healthy tissue for patients awaiting transplant. Second, bioartificial vascular networks can serve as models for disease and drug testing. Vascular pathology is implicated in many of the most common chronic human diseases including diabetes, hypertension, heart disease, and cancer[13]. The ability to make and study human blood vessels *in vitro* and *in vivo* could accelerate research into the basic biology of these diseases and enable the development of new classes of effective therapies. Last, engineered blood vessels can be used to directly replace damaged vasculature in human disease. Diseases of vascular insufficiency such as coronary artery disease, ischemic stroke, and peripheral artery disease may one day be treated by replacing or supplementing the native diseased vasculature with engineered vessels. Similarly, artificial vasculature could be used to aid in the healing of traumatic or surgical wounds.

While meeting important clinical needs in the overall population, engineered vasculature could also specifically address health disparities in disease burden[13] and organ transplantation[14,15]. For example, engineered vasculatures could be used to study the biologic consequences of racism that underlie disparities in response to hypertension treatment[16]. Despite similar rates of treatment, African Americans with hypertension are less likely to adequately respond to pharmacologic treatment and more likely to suffer complications such as stroke. Artificial *in vitro* vasculatures populated with patient-derived iPSC-endothelial cells could be used to develop more effective treatments for this population. The potential for engineered vasculature to address some of the most devastating and common human diseases, and the possibility of using artificial vascular networks to address health disparities demonstrates the importance of this technology.

1.3 HISTORICAL OVERVIEW OF ENGINEERED VASCULATURE

Early success creating artificial vessels was achieved with the creation of large (>4mm) tissue engineered blood vessels (TEBVs) consisting of synthetic membranes seeded with cells[17]. Since then, similar conduits have been fabricated using a variety of approaches including decellularized constructs[18], wrapping of cell sheets around a mandrel[1920], and bioprinting[21]. The progress in medium and large TEBVs has demonstrated the clinical utility of engineered vessels, which have performed favorably in human trials[22]. Despite the success of TEBVs, the development of vascular networks on the meso and microscale (<1mm) has remained a challenge. As we will primarily discuss vascular networks in this thesis, we refer the reader to other recent reviews with more in depth coverage of larger TEBVs[22,23].

Efforts to engineer vascular networks have used a combination of biology-driven and technology-driven approaches. Technology-driven approaches rely on sophisticated fabrication methods to generate artificial networks with defined topologic features. Techniques such as micro-molding, bioprinting, and multi-photon patterning have been used to fabricate artificial vasculatures with increasing fidelity to native vessel structure. Recent successes using these approaches can be found in the engraftment of bioprinted vessels *in vivo*[8] and in advanced microfluidic *in vitro* models[11]. Despite these groundbreaking advances, current technologies still fall short of replicating the complex, microscale 3D topologies of native vessels. In contrast to technologic fabrication methods which exert a high level of exogenous control over tissue structure, biology-driven approaches rely on natural cues to direct the formation of vascular networks. The observation that endothelial cells self-assemble into vessel-like networks *in vitro* and *in vivo* spurred the development of methods that rely on this process for vascularization[24,25]. The utility of self-assembly for vascular network formation has been demonstrated through the vascularization of engineered tissues *in vivo*[26,27] and more recently in self-assembled vascular organoids for *in vitro* disease modeling[9,10]*.* However, the inability to control the dimensions or organization of self-assembled networks often leads to irregular network geometries that bear little resemblance to healthy vascular beds. At the intersection of these approaches lie a variety of hybrid approaches that exert some level of top-down control over biology-driven network assembly. These strategies typically use biomaterials to deliver physical or chemical cues to direct vessel formation. By harnessing the power of biology to drive vascularization while maintaining control over vessel architecture, these hybrid methods fuse the advantages of purely technologic or biologic approaches.

We propose that successful engineering of vascular networks will require two key elements: 1) a comprehensive "blueprint" of vascular biology, topology and function; and 2) fabrication methods able to recapitulate these features in artificial networks. In Chapter 1, we first discuss what is known about the biology of vascular networks: how nature assembles these networks in the developing and adult organism, what the vessels in these networks are made of, and how close we are to achieving a comprehensive vascular "blueprint". Next, in Chapter 2 we review in detail the historical and recent progress towards engineered vascular networks and discuss how close this brings us to replicating the structural and biological features of natural vessels. Last, we highlight special topics for consideration that we believe will be critical to achieving biomimetic engineered vasculature.

1.4 FEATURES OF MULTISCALE VASCULAR NETWORKS

In this section, we discuss the process and outcome of natural vascular network assembly in embryonic development and regeneration. We review current and emerging knowledge of vascular topology, biology, and function and explore what is needed to achieve a comprehensive “blueprint” of the vasculature.

1.4.1 Evolutionary origins of blood vascular systems

All multicellular organisms must find ways to supply cells throughout their body with oxygen. Some simple organisms such as flatworms can rely on passive diffusion through the body wall to meet this need[12]. However, the slow rate of diffusion and limited penetration depth of oxygen through tissue places constraints on body size and metabolic rate. The evolutionary trend towards increasing body size required new systems to support tissue oxygen demands. In vertebrates the blood vascular system, a hierarchal system of branching tube-like structures, meets this need. Evidence points to the evolution of an early vascular system 600 million years ago[12]. While the first vascular systems were lined only with matrix, modern vertebrates have endothelium-lined vessels. The later emergence 540–510 million years ago of a vascular network lined with endothelial cells allowed additional control of barrier function, flow, and immune surveillance. Interestingly, the phenotypic heterogeneity of endothelial cells originated around the same time as endothelium itself, underlining the importance of endothelium in regulating vessel function to meet diverse tissue needs.[12]

1.4.2 Embryonic vessel formation

In mammalian embryonic development, vascular networks begin to form around the time of gastrulation[28]. In the initially avascular embryo, the first vessels must be created *de novo* from endothelial precursors in a process called vasculogenesis. In contrast, angiogenesis refers to the generation of new blood vessels from existing vessels. Both angiogenesis and vasculogenesis are involved in the establishment of a primitive vascular plexus in the developing embryo and in extra-embryonic tissue[29]. The basic steps of embryonic development have been conceptualized as follows: 1) formation of the primitive plexus, 2) stabilization of nascent vessels 3) remodeling and pruning and 4) vessel sub-type specialization[30]. The formation of the primitive vascular network begins when angiogenic precursors derived from the mesoderm aggregate to form "blood islands" comprised of angioblasts and immature blood cells. Next, the angioblasts begin to elongate, forming cord-like structures which then organize into capillary-like networks, establish lumens, and are endothelialized. The net-like vascular plexus is formed through sprouting angiogenesis, in which endothelial cells migrate and proliferate to form branches and loops. The process of sprouting angiogenesis is controlled by hypoxia-driven gradients of angiogenic factors including vascular endothelial growth factor (VEGF), angiopoietin-1, and nitric oxide synthase[30,31].

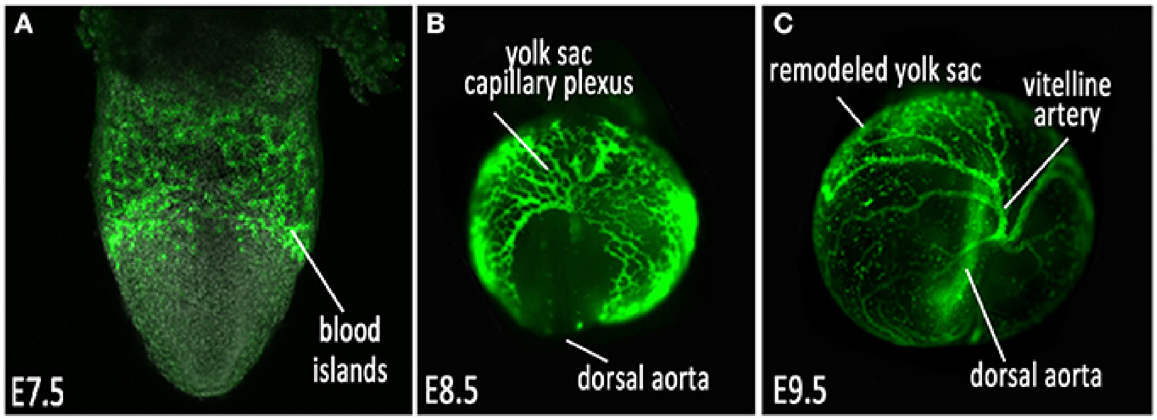

Figure 1.1 Formation of the early vascular plexus in the mouse embryo. The first step of vascular development is the formation of blood islands comprised of angiogenic precursors (A). Following the initial formation and stabilization of an immature vascular plexus (B), the network is remodeled and vessels undergo further specialization to establish a mature, hierarchical vascular network (C). Figure adapted from[32].

Following the establishment of a rudimentary vascular network, the initially leaky immature vasculature is stabilized, remodeled, and becomes specialized to meet the needs of different organs[30]. The recruitment of mural cells and changes in ECM composition stabilize and decrease leakage from the newly formed vessels[30]. After stabilization, the primitive plexus must be remodeled and pruned to meet local tissue needs. This involves both sprouting angiogenesis to supply additional vessels where tissue oxygen demand is high and pruning to dispose of redundant vessels in areas of low demand. The extracellular matrix is highly involved in the regulation of these processes, through the sequestration of growth factors to create local gradients, and through signaling pathways driven by integrin-matrix interactions[30]. The last step in vascular development is the specification of vessel subtype identity (artery, vein, capillary), as well as organ-specific microvascular specialization. Initially, it was thought that the specification of arterial and venous identity occurred only in response to hemodynamic forces following the initiation of flow[30]. More recent work indicates that vessel specialization begins even earlier, with the differential expression of arterial and venous markers preceding the first heartbeat[33,34]. Thus, it is now thought that both morphogen driven genetic markers and hemodynamic forces are required for the proper specification of arterial and venous identities[33]. The process of embryonic vascular development does not end following the establishment of vessel subtype and the onset of circulation. Rather, throughout the rest of embryonic development as well as during post-natal growth, the vasculature is continually remodeled to meet the increasing oxygen needs of growing organs.

1.4.3 Adult vessel formation

The primary mode of new vessel formation in adults is angiogenesis. In healthy states the adult vascular network is largely quiescent, with the exceptions of the female reproductive tract and during the response to injury[35]. In both these settings, the formation of new vessels is tightly regulated within a narrow spatial and temporal window. While angiogenesis is restricted in healthy states, aberrant angiogenesis occurs in several diseases including diabetic retinopathy, macular degeneration, and cancer[35]. And, while angiogenesis is the primary mode of new vessel growth in adults, vasculogenesis can also occur through the recruitment of endothelial precursor cells (EPCs) from the circulation[29]. Although the circumstances under which adult vasculogenesis occurs are still being fully defined[36], EPCs have been found to contribute to neovascularization in wound repair[37,38], tissue ischemia[39], and cancer[40].

The ability of adult endothelium to create new vasculature in response to injury is critical to wound healing. Upon tissue injury, the acute inflammatory response induces transient spikes in the levels of angiogenic factors such as VEGF, TGFβ, FGF, and angiopoietins, which promote angiogenic infiltration from the surrounding tissue[41]. As is the case in embryonic network formation, the ECM again plays a crucial role in the regulation of angiogenesis. In the early wound bed, the ECM is comprised of a fibrin/fibronectin clot, which is recognized by endothelial tip cells expressing the integrin receptor for fibrin, $\alpha v\beta 3$[41]. This interaction drives the formation of the transient and highly vascular granulation tissue that overlies the wound surface. The replacement of granulation tissue with a mature, avascular scar coincides with changes in ECM composition and structure from the early fibrin clot to a dense collagen matrix.

1.4.4 Immune contributions to embryonic and adult vessel formation

The immune system plays a key role in vascular network formation in both the embryo and the adult. During embryonic angiogenesis, yolk sac-derived macrophages are recruited to areas of newly forming endothelial junctions and act as cellular “bridges” that stabilize the fusion of these junctions[42,43]. In adults, pro-inflammatory macrophages recruited during wound healing associate with tip cells, the endothelial cells at the leading edge of a vessel sprout, and supply VEGF to drive neovascularization[44]. The clinical relevance of macrophage-driven angiogenesis is particularly evident in cancer, where tumor-associated macrophages (TAMs) can induce the malignant transformation from quiescent to angiogenic endothelium. TAMS induce this “angiogenic switch” at least in part by supplying matrix-degrading enzymes such as MMP-9 and angiogenic factors including VEGF[45,46]. The importance of macrophages to the growth of blood vessels in healthy and diseased states has informed efforts to develop anti-angiogenic therapies targeting TAMs[47]. In the future, it is possible that macrophages may also be strategically harnessed for pro-angiogenic applications, such as the vascularization of engineered tissues.

1.4.5 Features of arteries and veins

The mature vascular network contains a hierarchy of specialized vessel subtypes that are optimized for particular physiologic functions. This hierarchy can be divided into large vessels (arteries and veins, 0.1-10mm) which are responsible for transporting blood to and from the heart, and the smaller vessels of the microvascular circulation (arterioles, venules, and capillaries, 8-100μm)[48]. The large vessels have structural features that reflect their main function of bulk fluid transport. Both arteries and veins are comprised of three layers[48], but the composition of these layers differs between each vessel type and anatomic location. The innermost layer of all vessels is a single layer of endothelial cells called the tunica intima. The middle layer (tunica media) contains layers of smooth muscle cells and ECM components such as collagen and elastin. In most arteries and veins the medial layer also contains the bundle of nerves (nervi vasorum) that innervates the smooth muscle to control vessel tone. The outermost layer, tunica adventitia, is made up of collagen and elastin fibers that provide support to the vessel wall. Because the arteries receive blood directly from the heart, they have thick walls with elastin-rich medial layers to accommodate high pulsatile pressures. In contrast, veins typically have thinner walls because wall pressure is low as they return blood from capillaries to the heart. To maintain unidirectional within a low-pressure system, most veins have a series of one-way valves that protrude into the intima.

1.4.6 Microvascular heterogeneity

The structural heterogeneity found within the microvasculature reflects the wide array of functions that this system performs. The microvasculature consists of arterioles, venules, and capillaries. These microvessels perform diverse functions including the regulation of vascular resistance, gas exchange, tissue-specific barrier function, paracrine signaling to surrounding tissue, and immune surveillance. We will briefly discuss each of these functions.

Blood first enters the microvascular circulation in small arteries called arterioles. The primary role of arterioles is the regulation of vascular resistance, which allows the organism to match the rate of oxygen delivery with tissue demand[49]. Vascular resistance increases as blood moves from large arteries (0.1-10mm) into small arterioles (10-100μm), due to the inverse relationship between lumen size and resistance. This increase in resistance leads to substantial slowing of blood flow, thereby allowing sufficient dwell time for gas exchange in the capillaries. Resistance can be further controlled through the regulation of vessel tone (vasoconstriction or dilation) in response to autonomic innervation and hormones, allowing the organism to change blood flow patterns based on metabolic demands[49].

After the arterioles, the blood moves into capillaries and venules. The primary functions of these vessel types include gas exchange and barrier function, paracrine signaling, and immune surveillance. Gas exchange occurs in the capillaries, which have a single-layer endothelial wall through which diffusion of gases, ions, and small molecules can occur. While all capillaries allow gas exchange, differences in tissue-specific barrier function regulate the passage of other substances through the vessel wall[50]. On one end of the spectrum, the brain microvasculature is characterized by an abundance of tight junctions that form the highly impermeable "blood-brain barrier." In contrast, fenestrated capillaries in the kidney and small intestine have numerous small gaps (fenestra) between endothelial cells that allow increased permeability[50]. The capillaries with the highest permeability are found in the liver, bone marrow, and spleen[50]. The discontinuous capillaries in these organs have many large gaps in the endothelial lining, enabling the exchange of particles as large as blood cells.

Beyond organotypic barrier functions, the microvascular endothelium engages in crosstalk with the surrounding parenchyma and immune cells. It is now appreciated that organ-specific endothelial cells secrete growth factors, called angiocrine factors, that regulate the growth, patterning, and function of surrounding parenchymal cells[51]. These angiocrine factors are particularly important in injury response and regeneration, making them a potential target for the development of tissue engineering and regenerative medicine therapies. Last, the microvasculature has an important role in immune function, as it is the primary interface between the immune system and body tissues[52]. The microvascular endothelium aids in immune function by facilitating the adhesion and extravasation of leukocytes into the tissue, and by providing specialized microvascular niches for immune surveillance in the lymph nodes and spleen.

The importance of microvascular specialization is reflected in the increasingly appreciated phenotypic heterogeneity among endothelial and non-endothelial vascular cell populations[50]. Recent insights into the extent of endothelial heterogeneity have been uncovered through bulk and single cell transcriptomics studies, which have identified distinct transcriptional profiles of endothelial populations not only between organs but also within the same organ[2]. Increasingly, transcriptional heterogeneity can be correlated with functional heterogeneity across domains such paracrine signaling[51], metabolism[53], and immune regulation[54]. Beyond endothelial cells, specialization of non-endothelial cell types also contributes to tissue-specific microvascular identity. For example, organ-specific pericytes such as hepatic stellate cells in the liver and podocytes in the kidney perform specialized roles in tissue function and response to injury. The importance of these specialized pericytes is highlighted by their involvement in human diseases including cirrhosis and nephrotic syndrome[55].

1.4.7 Knowledge gaps

Despite our extensive knowledge of the formation, structure, and function of vessels in natural systems, we fall short of achieving a fully defined topological, biological, and functional 3D blueprint of the vasculature. To meet this goal, we as engineers and materials scientists must identify what features of vascular networks remain unexplored and develop tools to study these features. In this section, we will provide an overview of the technologies that inform our current understanding of vascular biology and highlight emerging methods that could address remaining gaps in knowledge.

The development of the compound light microscope allowed the first close study of vessel structure, enabling the discovery capillaries 1661[50]. In the centuries since this discovery, light microscopy of 2D histologic specimens has continued to provide the basis for our knowledge of vessel morphology, subtype, and ECM structure. A breakthrough in the understanding of micro-vessel ultrastructure came with the advent of electron microscopy in the 1950s and 1960s. This technology allowed the identification of sub-micron features of endothelium, including organ-specific differences in endothelial continuity[56]. While advances in electron microscopy, immunohistology, and high-resolution fluorescent microscopy have brought the field into the modern era, 2D histologic methods are inherently limited in their ability to capture complex 3D vascular architecture. `

The recent emergence of 3D fluorescent ultra-microscopy together with the revolution in ’omics technologies could fill current gaps in our understanding of vascular biology and topology. First, materials-driven advances in tissue preparation and imaging allow simultaneous visualization of multiple biologic targets within a 3D tissue at sub-micron resolution. In combination, clearing methods that render tissues optically transparent[1,3,57] and high-resolution confocal microscopy allow the 3D mapping of whole organ vasculatures with unprecedented detail[2]. Despite these important successes, traditional confocal microscopy is limited in resolution and burdened by the slow process of point-by-point laser scanning technology. A creative materials-driven solution to address resolution limits is expansion microscopy, which uses an expandable polymer to increase sample size prior to imaging[58]. Limitations in imaging speed have been overcome through the invention of ultra-resolution light-sheet microscopes[4,59], which can achieve imaging speeds of ~1 mm^3/min while maintaining sub-micron resolution[4]. A remaining challenge for large-scale 3D imaging is the storage and analysis of the resultant data sets, which can span tens to hundreds of gigabytes for a single tissue. For this technology to reach its potential as a mainstay of vascular biology research, there is a need for the development of streamlined, open-source, and user-friendly 3D visualization and analysis packages specifically designed for vascular biology applications.

In addition to advances in imaging, the emergence of spatial ’omics methods offer new tools to probe spatial heterogeneity within vascular biology. It is increasingly appreciated that cells exist in constant two-way communication with other cells, matrix components, and small molecules in their local environment. Untangling these complex relationships between cells and their environment requires methods that capture spatial information alongside ’omics data. Remarkable progress towards developing these methods has occurred with the explosion of spatial transcriptomic approaches, which most commonly use nucleic-acid barcoding of tissue sections to achieve sub-cellular resolution of RNA expression[5,6,60–62]. The *in silico* reconstruction of transcriptomes obtained from 2D sections can then be used to generate a 3D transcriptional atlas[63]. An alternative approach for 3D spatial transcriptomics can be found in STARmap, which uses polymer chemistry to incorporate tissues in a 3D hydrogel chip in which sequencing can occur, allowing direct read-out of spatial gene expression[64].

The power of 3D ’omics methods combined with 3D imaging methods paves the way for a multi-dimensional, annotated atlas of the topologic, cellular, and biochemical features of vascular networks that can serve as a blueprint for engineering artificial vasculatures. The continued refinement of these technologies and the development of analogous methods for spatially resolved proteomics, matrisomics, and metabolomics will move the field beyond the limitations of 2D methods and bring us closer to achieving comprehensive blueprint of vascular networks across organ systems.

CHAPTER 2. BUILDING VASCULAR NETWORKS IN ARTIFICIAL TISSUES

Our increasingly detailed knowledge of vascular network composition leaves us with the following question: what level of structural and biologic complexity is necessary for proper engineering of vascular networks? Answering this question requires consideration of what features of vascular networks can be specified using engineering technology, and in what situations we should relinquish control to biology-driven processes. In this chapter, we explore these questions of technology-driven vs. biology-driven approaches for generating vascular networks (Fig 2.1). Through this lens, we define the methods used to build vascular networks in artificial tissues, with a focus how materials have been deployed across different assembly methods. We first review engineering modes of fabrication that exert sophisticated control over network geometry but lack biological fidelity. Next, we contrast technology-dependent strategies with those that rely predominantly on natural mechanisms of vessel self-assembly. Last, we highlight emerging efforts that seek to bridge technological and biological modes of vascular network assembly.

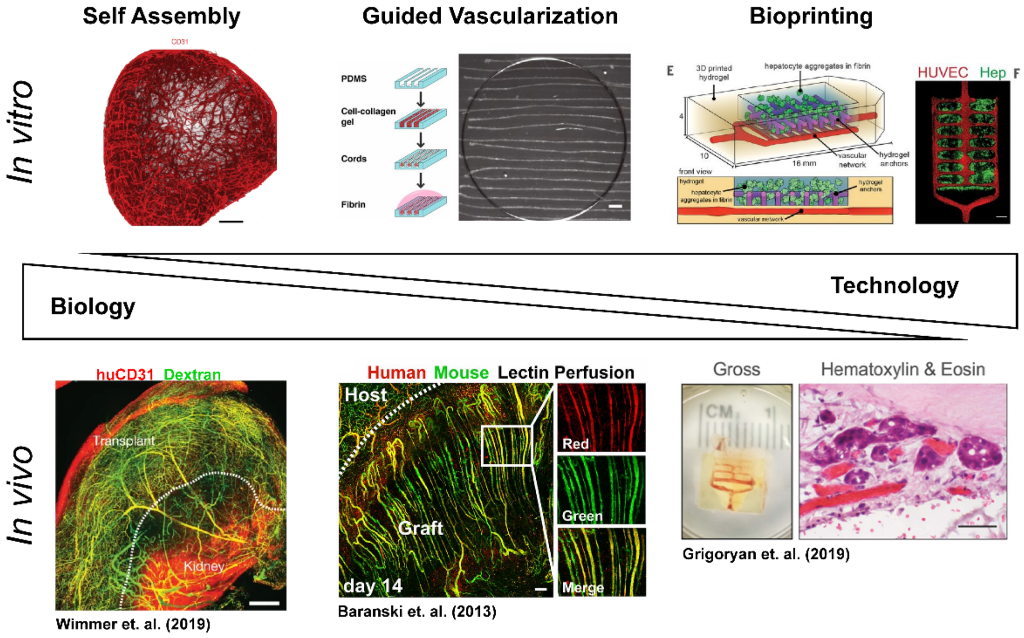

Figure 2.1 Examples of methods to engineer vascular networks across the biology-technology spectrum. On one end of the spectrum, self-assembled vascular organoids rely on biology to generate a vascular network (left) that becomes perfused *in vivo*[9]. A hybrid approach (middle) uses patterned endothelial "cords" to guide vascularization[65]. The technology-driven approach of stereolithographic bioprinting (right) allows full control over vessel structure *in vitro* and printed constructs become perfused with host blood *in vivo*[8]. These methods are described in detail in the following sections (2.1-2.3).

2.1 Bio-Fabrication and Additive Manufacturing

While the small diameter and hierarchical architecture of microvascular networks have proven challenging to replicate with conventional fabrication methods, recent technologic advances bring us closer to recapitulating the complex topologies of natural vessels. Here, we will provide an overview of historical and current technologies for the *in vitro* fabrication of artificial vascular networks.

2.1.1 Micro-molding and soft lithography

Some of the first approaches used to generate artificial vascular networks relied on micro-molding and soft-lithography technologies. An early example of these is needle-casting, in which a hydrogel is cast around a removable needle[66]. Upon polymerization, the needle is removed, leaving a channel that can be seeded with endothelial cells. Needle-casting enabled the creation of perfusable vessel-like structures *in vitro*; however, the dimensions and geometry of the needles limits this method to the creation of single or parallel arrays of straight channels.[59] In comparison, soft-lithography methods borrowed from the microprocessor industry enabled the creation of relatively complex perfusable microfluidic networks, accelerating the development of organs-on-chips for *in vitro* disease modeling and drug testing[67]. To create branching vessel-like networks, soft-lithography uses a patterned photo-resist to generate a poly(dimethyl siloxane) (PDMS) mold with perfusable micro-channels[68]. However, PDMS fails to provide the ECM cues of native vessel matrices. To overcome this shortcoming, alternative methods use PDMS stamps to create micro-molded channels within more appropriate natural matrices. For example, the Zheng group used a multi-step fabrication approach to incorporate a collagen based microfluidic network within a perfusable chip[69]. The *in vitro* network of capillary-like vessels formed by this approach could then be used to study vessel biology and disease or incorporated into tissues for *in vivo* applications[69,70].

A related approach is the direct photolithography of a photo-polymerizable hydrogel. Instead of indirectly molding PDMS from a patterned photoresist, tissues are constructed by direct photopatterning of the hydrogel in a layer-by-layer fashion.[71] The

Radisic group demonstrated the feasibility of this approach by building a cardiac tissue with integrated vessel-like network through layer-by-layer photo-crosslinking of a synthetic polymer. This artificial tissue, referred to by the researchers as “Angiochip”, was then surgically anastomosed by connecting the inlet and outlet channels with the femoral vein in rats[72]. Despite this and other important achievements, an inherent limitation of micro-molding, soft-lithography, and layer-by-layer assembly techniques is the inability to replicate the 3D, interconnected topologies of natural vessels. Still, these microfabrication techniques continue to be relevant, especially for *in vitro* studies of vessels and within the organ-on-chip field.

2.1.2 Replicating 3D topologies with multi-photon patterning and bioprinting

To address the limitations of 2D fabrications methods, technologies including multi-photon patterning and bioprinting have been developed and refined to achieve increasingly precise control over 3D vessel architecture. These approaches can be grouped into the subtractive methods of multi-photon degradation and sacrificial printing, and additive bioprinting technologies.

Prior to the application of multi-photon laser systems for vessel patterning, photopolymerizable polymers had been used to build artificial vessels within tissues using a layer-by-layer approach. However, these additive light-based methods suffer from poor resolution in the z-direction and are limited in design complexity. An alternative light-based approach with improved 3D patterning capability is the subtractive patterning of vessel networks within photo-degradable hydrogels[73]. The application of multi-photon lasers allows photodegradation to be localized to a single point in three-dimensional space, enabling the rastered creation of microchannel networks with arbitrary geometry down to the capillary scale[73,74]. Another subtractive approach for creating hollow tubular networks within engineered tissues is the 3D bioprinting of sacrificial inks[75–78]. In these methods, a sacrificial ink is extruded through a printer nozzle to build desired vessel geometry. This solid printed structure is embedded within a hydrogel and subsequently dissolved, leaving hollow channels in the shape of the printed network. Cells may be embedded within the printed bio-inks[77], or later seeded within the empty channels[75]. A variety of sacrificial inks have been used for this approach including carbohydrate-based glass[75], Pluronic F127[76,77], and gelatin[78]. Although these approaches can achieve complex 3D architectures, the difficult multi-step fabrication has limited the widespread application of sacrificial printing approaches for tissue vascularization.

Besides the indirect printing of vessels using sacrificial inks, other bioprinting technologies can directly print hollow channels using additive approaches. While constrains on resolution have previously limited the success of directly printed microvascular networks, recent breakthroughs in extrusion and stereolithographic printing methods may overcome these challenges[79,80]. An advantage of direct extrusion printing, which uses cell-laden bio-inks to assemble artificial tissues voxel-by-voxel, is its compatibility with a variety of synthetic and natural materials[81–83]. The ability to print with multiple materials simultaneously using multi-nozzle systems, and the development of natural bio-inks such as those made from decellularized ECM, may allow engineers to replicate the architecture of the native vessel matrix more closely[82]. Despite these advantages, until recently the several-hundred-micron resolution limit of extrusion bioprinting limited its application to the construction of relatively large (>1mm) diameter conduits. However, in the recently published update to their freeform reversible embedding of suspended hydrogels (FRESH) bioprinting method, Lee et. al used a dissolvable gelatin support bath to print collagen structures as small as 20μm[84]. This allowed them to create an artificial heart valve containing a perfusable multi-scale vascular network with lumens as small as 100μm in diameter[84].

Aside from extrusion bioprinting, stereolithography (SLA) printers offer a different approach to the construction of 3D vessel networks[8,85,86]. By projecting an x-y plane of light within a photopolymerizable hydrogel precursor, SLA printers can rapidly construct tissues in a layer-by-layer manner. Free from constraints of nozzle-based extrusion printers, light-based printing can theoretically achieve very high resolutions. However, the practical resolution of SLA printers was until recently impeded by the diffusion of light from the plane of illumination, limiting the ability to print the fine details and complex topologies of natural vascular networks[80]. The discovery that a biocompatible food-safe dye added to the pre-polymer bath could limit light diffusion has now enabled the creation of perfusable networks with previously unattainable topologies. Grigoyan et. al used their stereolithography apparatus for tissue engineering (SLATE) platform to model the interconnected 3-dimensional architecture of the lung alveolus, demonstrating the ability of this approach to recapitulate complex natural topologies. In this paper, the authors also demonstrated applications of 3D bioprinting for vascularization of artificial organs by printing an engineered liver tissue with an integrated branching tubular network. Upon implantation, this construct achieved perfusion with host blood[8].

While advances in bioprinting methods have generated great excitement about the possibility of “3D printed organs”, the field is still far from achieving the resolution required to create biomimetic microvascular networks. For example, while SLATE printing impressively replicated the morphology of the air sac and capillary plexus of the alveolus, the size of the alveolar model was more than ten time larger than the 200-500μm diameter of the natural human alveolus[87]. Thus, to successfully print microvascular networks with high fidelity, additional work is needed to further push the resolution limits of bioprinting methods.

2.1.3 Materials used for technology-driven fabrication methods

An important factor when considering the relative advantages and disadvantages of fabrication technologies is the materials compatibility of each method. In general, materials used to form the matrix of artificial tissues can be categorized as synthetic or natural polymers. Natural polymers such as collagen, fibrin, or decellularized matrix can provide additional biochemical and mechanical cues for embedded cells but are not compatible with all fabrication methods. Micro-molding[66], soft-lithography[88], and extrusion bio-printing[84] have been used successfully to create perfusable vessels within natural matrices. However, light-based methods such as layer-by-layer photolithography, multi-photon patterning, and SLA printing require the use of materials that can be photopolymerized, thereby limiting the compatibility of natural polymers with these systems.

Commonly, the hydrogels used for light-based fabrication methods are poly(ethylene glycol) (PEG) derivatives with photo-crosslinkable moieties, such as poly(ethylene glycol) diacrylate (PEGDA)[8,85,86]. However, while PEGDA and similar polymers have desirable mechanical properties, they lack the bioactive signals provided by natural ECM. To address this, materials scientists have functionalized synthetic polymers with natural ECM features such as RGD cell-adhesion moieties[89] and enzyme-degradable linkages[90]. A hybrid approach combining both natural and synthetic materials can also be used for technologies that are not inherently compatible with natural polymers. For example, the liver tissues created by SLATE printing were fabricated by printing a vessel-like network within a PEGDA/GelMA casing that was then infilled with a fibrin gel encapsulating hepatocytes[8]. These and many other examples point to the indispensable role of materials in the development of fabrication techniques for engineering vascular networks. The creative use of novel materials has been critical to technologic breakthroughs in this field: from the initial success of sacrificial “sugar-printing”[75], to the development of designer PEG derivatives[91], to the recent revolution in SLA bioprinting[8] through the addition of a food-safe dye. The continued exploration and development of novel materials will no doubt continue to drive future advances in fabrication technology.

2.2 DEPLOYING NATURE AS THE BUILDER

In contrast with the methods discussed above, another set of approaches for engineering vascular networks relies heavily on biological rather than technological processes to establish the topological features of artificial networks. Here, we will discuss the self-assembly of vascular networks for tissue engineering and vascular organoids applications.

2.2.1 Self-assembled vascular networks for tissue engineering

The emergence of methods for engineering vascular networks via self-assembly started with the observation that endothelial cells cultured in a 3D laminin/collagen matrix form tubular networks *in vitro*[24]*.* Later, it was shown that this process could be replicated *in vivo* by seeding endothelial cells in natural (fibronectin/collagen)[92] or synthetic (PLGA/PLLA)[93] hydrogel scaffolds implanted in immunodeficient mice. The resultant self-assembled endothelial networks anastomosed with host vessels and became perfused with blood. While these early studies demonstrated the potential of vascularizing artificial tissues with self-assembled networks, vessels derived solely from endothelial cells were unstable and prone to regression over time[25]. Because natural blood vessels are formed and stabilized through the association of smooth muscle cells or pericytes with the endothelium, it was hypothesized that including peri-vascular support cells might similarly stabilize artificial vascular networks. Confirming this hypothesis, Koike et. al reported that co-seeding mesenchymal cells and endothelial cells in a fibronectin/collagen scaffold enabled the formation of stably perfused graft-derived vessels *in vivo*[25]*.* Soon after this discovery, the relevance of self-assembled vasculature for tissue engineering was demonstrated through the creation of artificial tissues with stably perfused, graft-derived vascular networks[27,94–96].

2.2.2 Self-assembly for vascularized organoids

More recently, self-assembled networks have been used for *in vitro* applications in the organoid field. Organoids are self-organized 3D cultures of organotypic cells derived from embryonic or adult stem cells[97]. The ability of these microtissues to recapitulate many of the developmental, structural, and functional properties of organs *in vivo* offers new access to the close study of human development and disease[97]. Without a vascular network, organoid size is limited to approximately 150μm in diameter, beyond which the failure of oxygen to reach the interior of the tissue induces the formation of a necrotic core[98]. Additionally, avascular organoids are limited in their ability to accurately model organogenesis, since vascularization is a key process in the development of organs such as the liver[99], pancreas[100], and lung[101,102].

Most efforts to vascularize organoids *in vitro* have taken either a co-culture approach of mixing endothelial cells with organ-specific cells[103,104] or a co-differentiation approach using mesodermal precursors that can differentiate into vascular cell types during organoid maturation[9,105]. While both these methods enable the formation of endothelial tubular networks in cultured organoids, to date no group has achieved maturation and perfusion of these self-assemble networks *in vitro*[98]. However, multiple groups have demonstrated that *in vivo* implantation of these “pre-vascularized” organoids does lead to rapid perfusion of the pre-assembled vascular network and promotes organoid maturation[9,103,106]. The recent work by Wimmer et. al demonstrates the potential of *in vivo* vascular organoids to recapitulate native vessel architecture in healthy and diseased states[9]. In this study, iPSC-derived vascular organoids became perfused and matured into a hierarchical network containing arteries, arterioles, venules and capillaries upon implantation in the kidney capsule of mice[9]. When exposed to a hyperglycemic milieu, these *in vivo* vascular organoids recapitulated microvascular changes found in human diabetes patients[9]. This study illustrates the importance of *in vivo* cues for the maturation of self-assembled vascular networks. Elucidating these cues and replicating them *in vitro* will be required for the realization of fully vascularized “organ-in-a-dish” systems for high-throughput disease modeling and personalized medicine applications.

2.2.3 Materials for self-assembly of vascular networks

Materials used for self-assembled vascular networks are most often derived from natural polymers such as fibrin, collagen, decellularized ECM, and Matrigel. Scaffolds formed from these materials mimic the structure of the natural ECM scaffold, providing mechanical cues and facilitating cell-ECM crosstalk through integrin signaling and the binding of soluble angiogenic factors[107]. However, compared with synthetic matrix materials, these natural hydrogels can be difficult to manufacture and are subject to natural lot-to-lot variability. In particular, the organoid field’s reliance on Matrigel, a chemically undefined ECM mixture derived from mouse tumor cells, may contribute to issues of replicability[108]. Additionally, the complexity of many natural polymers makes chemical modification difficult, limiting the ability to further tune these materials for improved performance.

To address limitations of natural materials, it is desirable to develop fully defined synthetic materials that replicate the angiogenic features of the native matrix. An interesting recent development in this endeavor is the emergence of “dynamic hydrogels” which can rapidly change their viscoelastic properties in response to traction forces exerted by encapsulated cells, mimicking the mechanosensitive properties of natural tissues[109]. Wei et. al demonstrated that these cell-responsive, dynamic hydrogels facilitate self-assembled vascular network formation *in vitro* and *in vivo* by promoting contraction-induced integrin clustering[109]. This study points to the importance of two-way crosstalk between cells and their extra-cellular environment. Therefore, materials for engineering self-assembled vascular networks must not only provide appropriate mechanical and biochemical cues but must also adapt their physical and chemical properties in response to cell-provided cues.

2.2.4 Pros and cons of biology-driven vs. technology-driven approaches

Relying on natural stimuli to guide vascular assembly has both advantages and disadvantages compared with current methods for technology-driven fabrication. An advantage of technologic fabrication methods such as bioprinting is the high degree of control over vessel dimensions and geometry. Although the recent report of self-assembled arteries in vascular organoids *in vivo* demonstrates the potential for these systems to replicate vessel hierarchy[9], most self-assembled networks contain relatively uniform capillary to arteriole size vessels (5-20μm). Since current technologic fabrication methods are limited in their ability to produce very small vessels, the ability to form self-assembled capillary-scale networks represents an advantage of biology-driven approaches. On the other hand, the lack of geometric control over self-assembled vessel networks may lead to irregular structural features that do not resemble the organization of healthy vasculature. For example, self-assembled vessels rapidly anastomose with the host following implantation, but the tortuous geometries of these vessels make them prone to premature thrombosis[110,111]. The complementary strengths and limitations of technology-driven and biology-driven approaches highlight the need for strategies that combine the control over tissue architecture with nature's capacity to form rapidly perfusable microvascular networks.

2.3 TECHNOLOGY + NATURE

In the following section, we will describe approaches that fuse technology with biology – harnessing the power of nature to drive vascularization while tuning this process through the delivery of biochemical and physical cues.

2.3.1 Delivering biochemical cues to stimulate vascular infiltration

The formation of new vessels in the embryo and adult is driven by angiogenic growth factors such as VEGF, PDGF-BB, FGF, Ang-1, and others[30]. Thus, it was reasoned that delivering these factors in engineered tissues might similarly promote vascularization. Sustained delivery of angiogenic factors within engineered tissues was achieved using methods adapted from the microparticle and nanoparticle fields, which had already developed sophisticated methods for the controlled release of pharmaceuticals. Two primary strategies for delivering biochemical cues are the direct incorporation of growth factors within hydrogels via encapsulation or cross-linking[112], and the incorporation of loaded microparticles/nanoparticles in artificial tissues[113,114]. To mimic the pulsed delivery of growth factors during natural angiogenesis, materials can be tuned to achieve the timed sequential release of multiple factors[115,116].

A more targeted approach for delivering angiogenic factors is the use of stimulus-responsive materials. These materials release their growth factor payload in response to environmental cues such as pH, enzymatic activity, redox environment, presence of small molecules, or traction forces[117]. Alternatively, materials can be engineered to respond to external stimuli such as ultrasound[118,119], heat[120], light, or magnetic fields. This enables the remote-controlled delivery of biochemical factors *in vivo.* Since the uncontrolled expression of angiogenic factors is associated with pathophysiologic states such as myocardial infarction and cancer, restricting delivery of these cues to the targeted tissue at a specified time may prevent undesired off-target effects[121].

Biochemical cues can also be delivered through genetic engineering by transfecting cells with nucleic acid sequences encoding angiogenic factors. In an example of the marriage of cellular and gene therapies to promote vascularization, Matsumoto et. al. used an adenovirus to transfect mesenchymal cells with the $VEGF_{165}$ gene and injected these cells in ischemic rat hearts[122]. The rats receiving this pro-angiogenic therapy had smaller infarcts and improved cardiac function[122]. Genetic delivery using viral vectors such as adenovirus or lentivirus can achieve high transfection and stable expression, but concerning off target effects have been reported[123]. A potentially safer alternative is non-viral transfection using chemical carriers to deliver nucleic acids to cells within engineered tissues[124]. While synthetic polymeric or lipid carriers are most commonly used for non-viral gene delivery, natural polymers such as chitosan and collagen can also be used[125]. The next frontier of genetic approaches for promoting vascularization may be the *ex vivo* remote control of engineered gene circuits using stimuli such as heat[126] and light[127]. These approaches may soon allow continual exogenous control over vascular network formation even after tissue implantation.

2.3.2 Physical cues to stimulate vascular infiltration

During natural vessel formation, cells respond to mechanical cues from the extra-cellular environment including stiffness, shear stress, and alignment[128,129]. Here, we will discuss how engineers can manipulate these physical properties to direct vascular network formation in an artificial tissue.

First, tuning matrix stiffness within artificial tissues can allow control over endothelial cell behavior. While initial 2D studies indicated that angiogenic sprouting occurs more readily on softer substrates[130–132], this relationship is less clear in 3D[133]. The conflicting results in 3D studies may be explained by the difficulty in isolating material stiffness from other properties of matrix architecture. A common method of increasing hydrogel stiffness is increasing matrix density. Yet, while increasing density inhibits endothelial sprouting in 3D hydrogels[134], increasing stiffness independent of density has the opposite effect[135]. Beyond effects on angiogenic sprouting behavior, tuning matrix stiffness may also enable control over vessel structure. For example, Yamamura and colleagues found that stiffness independent of pore size or density controls the lumen size of self-assembled vessels in a collagen gel[136]. Stiff gels promoted the formation of larger, multicellular lumens whereas soft gels had dense, thin vessel networks[136]. The potential of matrix stiffness to regulate angiogenesis and vessel morphology can be used to control network assembly within artificial tissues. However, when selecting materials for promoting vascularization, engineers must consider how changing stiffness might affect other aspects of matrix architecture.

Vessels in the body are subjected to constant hemodynamic forces that are sensed by mechanoreceptors on the surface of endothelial cells. The response of endothelial cells to flow regulates many important vascular functions including vessel stability and angiogenesis. Therefore, replicating physiologic flow in artificial networks *in vitro* could improve endothelial function and better approximate healthy vessel biology. Laminar flow improves endothelial barrier function by signaling through the mechanosensor NOTCH1[137,138]. This flow-induced Notch signaling promotes vessel stability by regulating junctional integrity and suppressing proliferation[138]. Through this mechanism, flow can be used to stabilize leaky and immature artificial vessels *in vitro*[88]. In addition to regulating vessel permeability, flow and shear stress are also important determinants of angiogenic sprouting[139]. Controlling the force and direction of flow within vascular networks can induce or inhibit sprouting and direct the orientation of resultant sprouts[139,140]. Thus, strategic direction of flow within artificial networks can be used to pattern angiogenic growth. A remaining challenge is replicating physiologic flow patterns in artificial systems. Despite the complex flow patterns present in natural vessel networks, most systems for modeling flow *in vitro* have relatively simple geometries. Recent work exploring endothelial behavior within helical vessel constructs illustrates the need to better model complicated physiologic flow patterns *in vitro*[141]

Last, engineers can direct vascular network formation through the specification of macroscale and microscale topographic cues to direct cell behavior. On the macroscale, patterning endothelial cells with collagen into pre-formed “cords” enables control over resultant network geometry *in vivo*[65]. Upon implantation, the EC cords guide the formation of perfused, chimeric host-graft vessels along the axis of each cord[142]. Interestingly, the early vessel-like structures that initially appear during this process are reminiscent of similar structures recently reported to form in embryonic lumenogenesis[143]. Thus, it is possible that the EC cords aid vessel formation by mimicking ECM cues that guide vasculogenesis in the embryo. On the microscale, endothelial cells *in vivo* respond to microscopic topologic features of the underlying basement membrane[144]. Patterning similar microscale and nanoscale features in artificial matrices can change endothelial cell behavior such as orientation, elongation, and migration[145,146]. In the future, these macroscopic and microscopic patterning techniques could be combined to specify network and cellular geometry across scales.

2.4 CONCLUSIONS AND PERSPECTIVES

As we discussed in Chapter 1 of this thesis, new tools for studying vascular biology bring us closer to completing a 3D "blueprint" that fully captures the heterogeneity and complexity of the native vasculature. This presents the question: where do our current technologies fall short of reproducing the features contained in this blueprint? In this final section, we review how close current technology brings us to replicating vascular hierarchy, heterogeneity, and function across scale. Through this discussion, we highlight key areas where additional tools are needed to meet the goal of engineering biomimetic artificial vascular networks.

While attempts to engineer hierarchical vascular networks have often focused on reproducing dimensional hierarchy, it is equally important to replicate hierarchies of vessel structure and function. This will require us to engineer vessels with dimensions that range from several millimeters to <10μm, while simultaneously replicating appropriate vessel subtype morphology. For example, arteries are defined not only by their size (>1mm), but also by their elastin and SMC-rich medial layer that can withstand high pulsatile pressures. Capillaries, in comparison, have single-layer endothelial walls to allow gas exchange. Thus, an engineered 1mm “artery” with the thin wall structure of a capillary will likely fail to perform the physiologic functions of either arteries or capillaries. Recent breakthroughs in multi-photon and bioprinting systems bring the field closer to achieving hierarchies of scale, but have not yet been able to replicate appropriate vessel subtype morphology[74,80]. Methods for self-assembly may better recapitulate morphologic features of vessel subtypes[9]; yet self-assembled approaches are limited by the lack of control over vessel dimensions. In the future, approaches that fuse the dimensional control of bioprinting with the biologic fidelity of self-assembled vessels could enable the creation of artificial vascular networks with physiologic function.

Another challenge is replicating the cellular heterogeneity of the native vasculature. Historically, engineers have often relied on readily available primary endothelial cells such as Human Umbilical Vein Endothelial Cells (HUVECs) as a cell source for artificial vessels. However, the increasingly appreciated role of organ-specific endothelial function has motivated the field to seek more biologically appropriate cell sources. Organ-specific primary human endothelial cells are difficult to obtain, limiting their clinical relevance. A more viable source may be patient-derived iPSC-derived endothelial cells. To replicate tissue-specific functions, iPSC-derived endothelial cells can be directed to acquire organotypic phenotypes through *in vitro* differentiation protocols or through *in vivo* specification in an appropriate tissue environment[147]. An alternative approach to iPSC technology is the direct reprogramming of normally quiescent adult endothelial cells to an angiogenic phenotype[148]. This approach can be used with endothelial cells from a variety of organs, although it remains to be seen whether these reprogrammed cells fully retain their organ-specific phenotype. While most attention has been paid to endothelial cell sourcing, replicating the phenotypic heterogeneity of non-endothelial cell types is also important. Defining appropriate cell sources for pericytes, fibroblasts, and SMCs will be necessary for capturing the cellular diversity of natural vessels.

As the field moves closer to replicating the structural and cellular features of natural vessel networks, it is important to consider whether artificial vessels achieve physiologic function. Flow is a common benchmark used to assess vessel function *in vivo*. Methods for visualizing flow each have unique advantages and disadvantages[149]. When choosing a method for assessing flow, it is important to consider the research question being asked. For example, when assessing temporal questions such as when flow is established, it is useful to select a method that allows for easy serial imaging. If the tissue being studied can be implanted superficially, intra-vital microscopy with a surgically placed optical window might be a useful approach. If instead one wants to determine whether *in vivo* flow rates in an artificial cardiac patch are comparable to physiologic flow rates, methods that with deep tissue penetration, such as microCT, are required. While measuring flow is important, it does not capture the range of physiologic functions performed by the vasculature including gas/nutrient exchange, response to vasoactive stimuli, and paracrine function. Thus, to determine the relative success of a vascularization strategy, we must find ways to comprehensively assess multiple functional capacities simultaneously.

Importantly, the goal of generating artificial vascular networks for tissue engineering applications is to support tissue function *in vivo.* To accomplish this goal, all engineering needs to be done in the context of supporting the tissue and integrating it with the host. Therefore, we not only need improved fabrication methods to better replicate vascular structure, but we also need a deeper understanding of how host biology influences tissue integration *in vivo*. In the following chapters we will focus on the importance of understanding and optimizing host biology for the success of tissue engineering efforts.

2.5 THESIS MOTIVATION AND OVERVIEW

To successfully address the need for vascularization in engineered tissues, a deeper understanding of the influence of host biology in this process is needed. Although an array of methods for engineering vasculature have been developed, there are few studies comparing the performance of these strategies in different host environments. The goal of this thesis is to address this knowledge gap by studying the *in vivo* integration of a bioartificial tissues containing endothelial "cords" across implant locations (intra-peritoneal and supra-epicardial) and species (athymic rats and athymic mice). We chose the EC cords system for two reasons. First, geometric specification of endothelial cells in this way has previously been shown to improve vascularization and function of engineered liver tissues in the mouse abdomen[65,150]. Second, we hypothesized that EC cords, if they functioned similarly in the heart, could "guide" vascularization from healthy tissue into a patch placed over an infarcted area of myocardium.

To test whether EC cords could vascularize cardiac tissues as well as liver tissues, we implanted cords patches on the supra-epicardial surface of athymic rat hearts (Chapter 3). We chose athymic rats for our initial experiments because their relatively larger hearts compared with mice make them a common model for cardiac tissue engineering applications. Similar to previous studies[65,142], we found that EC cords on the rat heart formed patterned clusters of large blood-filled lumens at 3 days[151]. However, unlike the persistent patterning reported in the mouse abdomen, in the rat heart we found that patterning of graft-derived vessels was lost by 7 days post-implantation. This loss of patterning was associated with marked inflammation, patch degradation, and collagen deposition. Based on this finding, we next sought to understand whether an implant location difference or species difference could explain the aberrant host response in the rat heart compared to the mouse abdomen.

In Chapter 4 of this thesis, we compare vascularization and host response to EC cords patches implanted across anatomic locations (intra-peritoneal (IP) and supra-epicardial) and in different species (athymic mice and athymic rats). First, we compared cords-containing tissues implanted in either IP or supra-epicardial sites in athymic nude mice. At 7 days, we found patterned blood-filled microvessels and minimal inflammation in tissues from both implant sites, suggesting that guided vascularization had occurred in both locations. We next studied species differences by comparing the host response of athymic nude mice and athymic nude rats to a cardiac patch containing human pluripotent stem cell derived cardiomyocytes (hCMs) and EC cords. While the cardiac tissues in mice formed tracts of human microvessels recapitulating cords geometry, the graft-derived vessels in rats had lost geometric patterning. Despite the apparent inflammation however, rats supported larger human cardiac grafts than mice. These data highlight the importance of host biology in determining vascularization and tissue integration. Additionally, the superior cardiomyocyte engraftment in rats despite a lack of patterned vasculature suggests that guided vascularization and cardiomyocyte engraftment are controlled by different host factors. It will therefore be important for the field to untangle the specific host factors that optimize each of these processes.

The work presented in this thesis challenges the assumption that strategies for engineering vasculature can be easily transferred across applications and model systems. Instead, we have shown that a vascularization method with patterned EC cords leads to dramatically different responses in athymic nude rats compared to athymic nude mice. This finding is important for the field because as technologies are brought through pre-clinical and clinical trials, they are typically tested in multiple species throughout development. Without a better understanding of host differences, a technology that works well in mice may fail in larger animals or humans. Future research is needed to better understand the specific micro-environmental cues that aid vascularization, and to develop host-responsive strategies for tissue engineering.

CHAPTER 3. GUIDED VASCULARIZATION IN THE RAT HEART LEADS TO TRANSIENT VESSEL PATTERNING

3.1 ABSTRACT

Recent progress in the production and maturation of iPSC-cardiomyocytes has facilitated major advances in building bioartificial heart tissue with functional cardiomyocytes. Despite this progress, vascularizing these constructs continues to be a barrier to clinical application. One emerging strategy for vascularization uses aligned "cords" of endothelial cells in tissue grafts to guide assembly of chimeric microvessels upon graft implantation. Here, we test whether this approach can guide vascularization of a bioartificial tissue implanted on the rat heart. We find that patterned "cords" of human endothelial cells anastomose and become perfused with host blood by 3 days post-implantation. Immunohistochemical staining confirmed that graft-derived micro-vessels persist in the patch at 7 days. Furthermore, we noted a shift in distribution of vessels in the patch from patterned cords-associated clustering at 3 days, to a more diffuse distribution pattern at 7 days. This loss of patterning corresponded with an infiltration of CD68+ cells and an increase in collagen within the patch. Upon further engraftment of patches containing both cords and human cardiomyocytes, we identified human cardiomyocytes and graft derived vasculature at the time of explant. These findings show that patterned endothelial cords guide transient vessel patterning on the rat heart. Our results also suggest that future work should be directed at further adapting vascularization strategies to the epicardial environment, and add to an important emerging dialog in cardiac cell therapy that points to the need to characterize host response prior to or in parallel with efficacy studies.

3.2 INTRODUCTION

The only definitive treatment for end stage heart failure is replacing the damaged muscle via heart transplant. However, the supply of transplantable organs is limited in comparison to the number of patients who could benefit from transplant[152]. For patients who do not have access to a deceased donor heart, bioartificial cardiac tissues offer a promising alternative source of implantable human myocardium. Recent advances in scalable production and maturation of pluripotent stem cell derived cardiomyocytes have brought this technology closer than ever to clinical translation[153–158]. A remaining obstacle is the inability to generate a dense, host-perfused vasculature that can support oxygen and nutrient exchange for implanted cardiomyocytes[159], without which tissue thickness is limited by the diffusion limit of oxygen, preventing the creation of human-scale tissues for clinical applications.

Early success towards vascularization by us[27] and others[94] was achieved through homogenously seeding endothelial and supportive stromal cells into engineered tissues, which led to self-assembled tubular networks that became perfused upon implantation[27,94]. However, some subsequent studies have suggested that the disorganized and tortuous nature of self-assembled networks may make them susceptible to thrombosis[111]. Therefore, we and others have worked to develop methods to more precisely control geometry of engineered vascular networks[65,70,142]. One such method is micropatterning endothelial cells and stromal cells along with collagen to form aligned cord-like structures[65]. We showed that such endothelial cords improved vascularization and function of bioartificial liver tissues implanted in the mouse abdomen by guiding host vessel ingrowth and decreasing time to perfusion[150]. This method of vascular patterning could be appealing in the context of the injured heart, as the cords may be able to recruit vasculature from the peripheral healthy tissue into the hypovascular infarct zone. However, it is not known whether cords can guide vascularization in the environment of the supra-epicardial surface, where an engineered tissue patch would be applied. Therefore, we sought to determine if cords could guide vascular infiltration of a bioartificial tissue patch applied to the surface of the rat heart.

Here, we demonstrate that endothelial cords embedded within fibrin hydrogel induce formation of aligned micro-vessels supra-epicardially on the rat heart. We found early anastomosis and patterning of nascent human derived blood vessels within these tissues. However, we also observed a robust host response and loss of architectural vascular patterning over time. Thus, this work suggests that guided vascularization may be a useful strategy for cardiac tissue engineering and informs future directions in adapting vascularization strategies for grafting on the epicardium.

3.3 METHODS

3.3.1 Cell culture and fabrication of cords patches

Human Umbilical Vein Endothelial Cells (Lonza, P2-P4) were cultured in EGM-2 media (Lonza) on tissue culture treated poly(styrene). Mouse mesenchymal stem cells CH310t1/2 (ATCC, P4-P7) were cultured in low glucose Dulbecco's Modified Eagle's Medium (DMEM) supplemented with 10% v/v fetal bovine serum (FBS, BioWest). Media was replaced every 48 hours and cells were passaged or used for experiments at 80% confluence.

Patches containing endothelial cords were fabricated as previously described[65,142]. Briefly, a PDMS mold patterned with a parallel array of 150 μm channels was treated for

5 minutes with 0.02% Pluronic F-127 and subsequently rinsed with PBS. HUVECs and CH310t1/2 cells were resuspended at a 50:1 ratio in liquid 2.5% collagen neutralized to pH 7.4 and seeded into the channels by centrifugation. For each cords mold, 2 million HUVECs and 40,000 CH310t1/2s were used. Excess collagen was aspirated from the molds, leaving the cell/collagen mixture only in channels. The molds were then incubated for 8 minutes at 37°C to allow collagen polymerization. Then, a drop of EGM-2 media (Lonza) was carefully introduced on top of the cords and the constructs were returned to incubate for 3 hours. Following cord contraction, the molds were inverted onto a PDMS gasket containing 150µl of 10mg/mL fibrin which was allowed to polymerize for 5 minutes at 37°C. Next the molds were peeled away, leaving the cords embedded in the fibrin. A second layer of fibrin was added to fully encapsulate the cords. To obtain patches for implantation, punches from the larger construct were taken with a 6mm biopsy punch.

3.3.2 Maintenance and differentiation of pluripotent stem cells

Human iPSCs (WTC-11, Coriell) were maintained on Matrigel (BD Biosciences) coated plates with mTeSR-1 (Stemcell Technology). Small-molecule modulation of the Wnt pathway[160] was used to differentiate cardiomyocytes. Briefly, iPSC’s brought to a single cell suspension were seeded at a density of 42,000 cells/cm^2 in Matrigel coated plates with mTesR containing 10 µM Y-27632 (Stemcell Technology). After 24 hours, media was changed to mTesR with 1 µM Chiron 99021. 24 hours later, media was changed to RPMI 1640 supplemented with B27 (minus insulin) containing 5 µM Chiron 99021. After 48 hours, cells were rinsed with PBS and media was changed to RPMI 1640 supplemented with B27 (minus insulin) containing 2 µM Wnt-C59. After an additional 48 hours, media was replaced with RPMI 1640 supplemented with B27 (minus insulin) without additional small molecules. 48 hours later the media was changed to the final “cardiomyocyte media” (RPMI supplemented with B27 containing insulin). From this day forward, cardiomyocyte media was replaced every 48 hours. Beating clusters were observed starting on approximately day 9 of differentiation. On day 14, cells were replated on Matrigel-coated plates. Lactate selection with DMEM (no glucose) supplemented with 4mM sodium lactate was performed between day 18-22[161]. Cardiomyocytes were used at D28 post differentiation.

3.3.3 Supra-epicardial implantation of patches on athymic rat hearts

All animal procedures were approved by the University of Washington Institutional Animal Care and Use Committee (IACUC protocol #4388-02). Male athymic nude Sprague-Dawley rats (Envigo, 150-220g) underwent thoracotomy to implant 2, 6mm patches on the supra-epicardial surface of the heart. First, animals were induced with 5% inhaled isoflurane, orotracheally intubated, and maintained on 2% isoflurane. A left lateral thoracotomy was performed and the chest was held open with retractors to expose the heart. After removing the pericardium, patches were affixed to the supra-epicardial surface using 8-0 suture. The chest was closed and animals recovered until they were able to move about freely. Analgesia was provided during the first two days with a subcutaneous injection (1mg/kg) of slow releasing buprenorphine. For patches that contained cardiomyocytes, daily subcutaneous injections of Cyclosporine A (5mg/kg) were administered for 7 days, beginning on the day prior to tissue implantation.

3.3.4 Tissue harvesting, processing, and 2D histology

Animals were sacrificed at the appropriate timepoints via intra-peritoneal injection of pentobarbital/phenytoin solution (Beuthanasia; 1.5 mL injection) and the heart was removed. Explanted hearts were processed for histology by fixing in 4% (vol/vol) paraformaldehyde (PFA) for 48 h at 4 °C, progressively dehydrating the tissue with ethanol, and embedding in paraffin. Blocks were sectioned using a microtome (5 μm) and collected on charged slides. Overall tissue morphology was visualized with hematoxylin and eosin (H&E). Collagen structure was identified by staining with Picro Sirius Red (Direct Red 80, Sigma) using Fast Green (Sigma) as a counterstain. For immunostaining, heat mediated antigen retrieval in pH 6.0 sodium citrate buffer was performed, and sections were blocked with normal goat serum (5%). Overnight incubation of primary antibodies was performed at 4 degrees using antibodies against human CD31 (1:20, Dako), hemoglobin A (1:100, Abcam), or beta-myosin heavy chain (hybridoma supernatant, ATCC #CRL-2046, full strength). For brightfield peroxidase-based visualization of huCD31 and CD68 (1:100, Abcam), we used either anti-mouse or anti-rabbit specific Avidin/Biotin complex (ABC) detection kit (AbCam). For fluorescence visualization, hemoglobin A was detected with 1:500 IgG (H+L) Highly Cross-Adsorbed Donkey anti-Rabbit secondary Alexa Fluor® 488 (Invitrogen) and β-MHC or huCD31 were detected with 1:500 Novex Goat anti-Mouse IgG1 Secondary Antibody, Alexa Fluor 555 conjugate. Fluorescent images were acquired on a Nikon Eclipse Ti inverted microscope with either Photometrics CoolSNAP HQ2 camera for widefield images, or Yokogawa W1 spinning disk confocal head and Andor iXon Life EMCCD camera for confocal images. H&E, Sirius Red, and DAB stained slides were scanned with an Aperio ScanScope AT2 digital whole slide scanner.

3.3.5 Retrograde perfusion, Clearing and 3D Imaging

For studies of 3D vessel structure (lectins and OMAG) n=3 rats per group (n=3 for lectin, n=3 for OMAG) were implanted with cords patches containing cardiomyocytes, HUVECs, and Normal Human Dermal Fibroblasts (NHDFs) in the bulk fibrin. On day 7 post-implantation, rats were sacrificed, and hearts were fixed by retrograde perfusion. First, rats in a deep plane of anesthesia (5% isoflurane) were administered 50U Heparin via the inferior vena cava. The heparin was allowed to circulate for 1 minute and the heart was then removed and submerged in saturated KCL solution. Next, the heart was cannulated through the aorta and flushed with vasodilation buffer (PBS containing 4 mg/L Papaverin and 1 g/L adenosine) until no blood was apparent in the effluent. To visualize vessels, 50 µg/mL DyLight 649 labeled Lycopersicon Esculentum (Tomato) Lectin (LEL, TL) in vasodilation buffer was perfused for 10 minutes through the hearts. Hearts were then fixed by perfusion with 4% paraformaldehyde and either used the same day for OMAG or left in fixative overnight. The next day, hearts were rinsed in pbs and incubated with blocking solution (0.1M Tris, 1% BSA, 1% Normal Donkey Serum, 0.3% triton x-100) for 6 hrs at 37°C. Then hearts were transferred to blocking solution with 1:100 human specific CD31/PECAM-1 DyLight 550 conjugated antibody (Clone: JC/70A, Novus) for overnight incubation at 37°C, shakings. Following staining, hearts were cleared with the Clearing Enhanced 3D Microscopy (Ce3D) protocol at 37°C for 48hrs[162]. Cleared hearts were imaged with a Leica TCS SP8 confocal laser scanning microscope.

3.3.6 Optical Microangiography

Hearts that were visibly well perfused (intralipid filling small vessels) were used for OMAG imaging. The tissue was prepared for optical microangiography (OMAG) imaging following the protocol established by Qin et. al.[163] Briefly, the hearts were retrograde perfused with 4% PFA and then left in a bath of PFA for 1 hour prior to imaging. Prior to imaging, a 10% intralipid solution was perfused through the heart at a constant pressure of 120mm Hg for 20 minutes to equilibrate. After 20 minute equilibration, the heart was placed onto a translating imaging stage and raised to the focal plane of the OCT imaging arm. The swept-source OCT (SS-OCT) system employed in this study has been previously reported in detail.[164] Briefly, a 200-kHz vertical-cavity surface- emitting (VCSEL) swept laser source (SL1310V1-10048, Thorlabs Inc., Newton, NJ) with a central wavelength of 1305 nm (spectral bandwidth of 100 nm) was utilized, providing an axial resolution of ~8 μm in tissue (~11 μm in air). The power of the incident light on the sample was measured at ~5mW, providing OCT sensitivity of ~105 dB. For this study, an 18mm effective focal length lens (LSM02, Thorlabs Inc.) was used, resulting in ~10um lateral resolution. 3D volumetric scans were acquired with a field of view (FOV) of 4mm x 4mm and a penetration depth of ~1.5mm. The beam spot was scanned with a paired X-Y galvo scanner (6210H, Cambridge Technology, Bedford, MA), forming raster sampling patterns comprising fast (x-axis) and slow (y-axis) scans. At each y-location, 400 A- scans were acquired to create a single B-frame. 8 B-frames were repeated before moving to the next y-location. Following this protocol, a single 3D volumetric scan (C-scan) was generated (a detailed analysis of typical OMAG scan sequence was previously reported by Deegan, et. al.[165]). The repeat frames were used to generate the optical microangiography

(OMAG) image based on eigen decomposition analysis[166]. The basis of this technique allows repeat B-frames to provide a 3D volume image contrasted by particles in motion. The scan protocol was designed to contrast capillary vessels with a minimum flow rate of 0.1mm/s. The resulting ED-based OMAG signal thus identified regions where intralipid was flowing through microvessels faster than .1mm/s[167]. In this case, the intralipid solution flowing in the microvessels provides 3D contrast of the vascular structure. The method resulted in a co-registered image of both static (tissue) and dynamic (intralipid) components providing information on both local tissue and vascular structure.

The 3D structure and vascular images were captured on both healthy tissue and within the patch region. For visualization, the 3D data was compressed to maximum intensity projected en-face vascular images, with ED-signal above a 5dB threshold displayed and mapped to a color based on depth[165]. The 3D data was cropped at approximately 450 microns below the tissue surface to remove any signal from beyond the vascular wall. A 10mm fov charge-coupled device (CCD) camera co-aligned with the OCT imaging arm captured visible light images to align the OCT images with the patch and healthy heart region.

3.3.7 Quantitative Tissue Morphometry

For the purposes of analysis, patch area was defined as the area spanning from the epicardial surface of the rat heart to the outer edge of the patch. Nuclear density was quantified in FIJI using the color deconvolution and automatic cell counter tools to isolate the hematoxylin and eosin stains and count hematoxylin positive nuclei within the patch area respectively. For quantification of CD31 and HgbA area, a biologically relevant threshold was selected and applied uniformly to all images in each set, and the percent area of the patch positive for each stain was calculated.

For analysis of CD68+ area, images from each scanned slide were generated to represent three distinct regions of tissue. First, the patch area was defined as the region from the epicardial surface of the rat heart to the boundary of visible tissue. Second, the patch-heart interface was defined as the 300 μm of heart tissue underlying the patch. Lastly, a region of healthy heart was selected from heart tissue on the opposite side of the sutures. Images from these three regions were separated into stained and unstained regions using the segmentation tool Ilastik. The stained and unstained regions were converted to binary masks from which percent of stained area was calculated[168].

For quantification of huCD31 and LEL positive area within 3D stacks, each frame was separated into stained and unstained regions using Ilastik. The stained and unstained regions were converted to binary masks from which percent of stained area was calculated[168]. Quantified data from 3 animals was averaged and plotted with a custom python script. 3D volumes were visualized using ChimeraX[169].

3.3.8 Nearest Neighbor Analysis

Images of hematoxylin and eosin (H&E) stained explanted grafts were acquired and preprocessed using the FIJI 'deconvolve' function to isolate the eosinophilic red blood cell signal. The corresponding signals were thresholded and converted to binary masks. A custom python script was used to perform a distance transform of each binary mask. The output of the distance transform is an array with each pixel's intensity corresponding to its distance away from background in the respective binary mask. The pixels corresponding to the local maxima of the distance transformed binary masks were used as indices for individual red blood cells. A graph was then constructed with nodes representing single red blood cells and edges with weights corresponding to the Euclidean distance between the two nodes (red blood cells) they connect. The corresponding adjacency matrix was used to find the minimum distance to a neighboring cell for every cell in the image.

Images acquired after immunostaining explanted grafts for human CD31 (huCD31) and staining with Hoechst were preprocessed using a morphological top-hat transformation to reduce background noise. huCD31 channels and the Hoechst channels were then isolated from the background corrected images. The individual channels were thresholded and converted to binary masks. A distance transform was performed on the Hoechst channel masks. The local maxima of the distance transformed masks were used as cell nuclei indices. These indices were then used to check for colocalized huCD31 signal and mark huCD31-positive cells. A graph was constructed with the nodes representing single huCD31-positive cells and the edges representing the Euclidean distance between the two nodes (huCD31-positive cells) they connect. The graph's adjacency matrix was used to find the minimum distance to a neighboring cell for every cell in the image.

3.3.9 Statistical Analysis

Graphpad prism software was used to compare the three groups using one-way ANOVA with Tukey's HSD as the post-hoc test. Error bars are reported as standard error of the mean. For *in vivo* experiments, the sample size represents the number of animals in each group.

3.4 RESULTS

3.4.1 Culture of endothelial and stromal cells in microchannels facilitates formation of "cords"

We first cultured human umbilical vein endothelial cells (HUVECs) and a stromal cell population (CH310t1/2) within 2.5% collagen in PDMS microchannels 150 μm in width and 100 μm in height as published previously[65]. We found that after a 3-hour incubation within the channel molds, cells compacted to form aligned "cords" with approximately half the diameter of the original channels (Fig 3.1A). Second harmonic generation microscopy[170] demonstrated that compacted cords consisted of a loosely consolidated collagen core, with cells adhered around the periphery (Fig 3.1B). We encapsulated cords within a fibrin hydrogel to generate implantable bioartificial tissues and used a 6mm biopsy punch to generate patches for implantation (Fig 3.1A)[142]. We confirmed cellular viability of encapsulated cords by staining for live and dead cells at the time of implantation (Fig 3.1B, bottom).

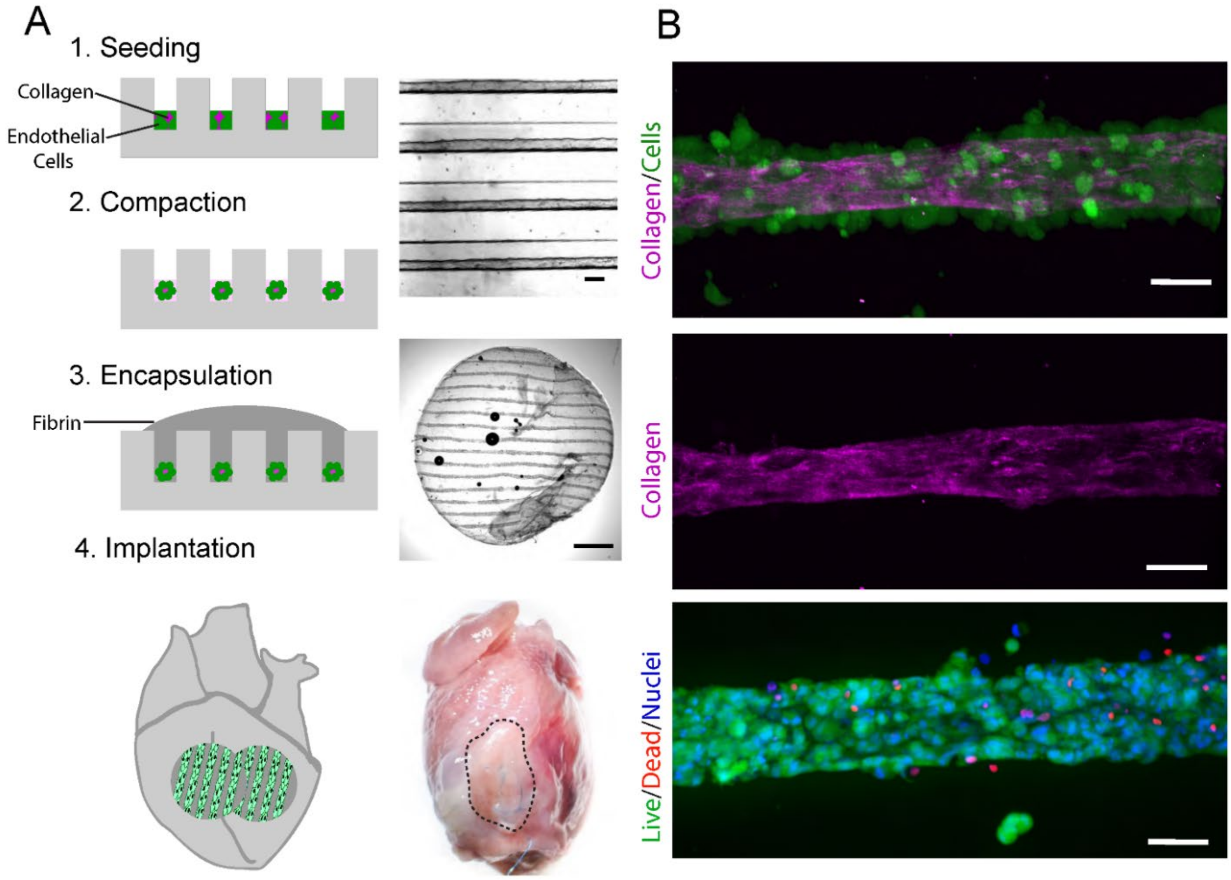

Figure 3.1 Generation of patches containing "endothelial cords" for epicardial implantation. (A) Fabrication of patches by molding of endothelial cords, encapsulation in fibrin, and implantation on the supra-epicardial surface of an athymic rat heart. Scale bar (top) = 50 µm. Scale bar (middle) = 1mm. (B) *In vitro* characterization of cords with staining of live (green; calcein) and dead (red; ethidium homodimer) cells, and second-harmonic generation microscopy to visualize collagen (pink). Scale bar = 50 µm.

3.4.2 Cords induce guided vascularization on the uninjured rat heart

We next sought to determine if bioartificial tissues containing micromolded endothelial cords could become vascularized on the heart, as we found previously when similar constructs were implanted in the abdomen of mice[142,150]. To characterize vascularization of cords-containing tissue we implanted patches supra-epicardially in athymic rats and harvested the hearts at 1, 3, 7, and 14 days post implantation. After 7 days and 14 days of implantation, we noted fibrous adhesions between the heart and the chest wall, which we carefully dissected away to free the heart for explant. Patches were located by visualizing the suture knot on the exterior of the heart through seven days of engraftment. While we were able to locate the implanted patches by identifying suture at 14 days, no patch was evident by gross examination so we did not further analyze this timepoint. Using routine histological analysis of patch sections with Hematoxylin and Eosin (H&E), we clearly identified a linear array of cords cross-sections that were surrounded by pools of blood at 3 days (Fig 3.2A, center panels). Upon examination of individual cords, we found numerous, large blood-filled lumens arranged circumferentially around a central point. The blood pools were not apparent at the 7 day timepoint. Instead, we noticed a subset of cords associated with small, <10μm microvessels (Fig 3.2 A). The cord cross-sections at 7 days had a characteristic eosinophilic, acellular core with micro-vessels situated peripherally around this core. We also confirmed identification of cords-associated micro-vessel formation with Sirius Red/Fast Green staining, in which micro-vessels were visualized as tight consolidations of blood (yellow) at the periphery of a collagen core (red) (Fig 3.2 B, inset). We and others have shown that cord-associated blood pools mature to form stable microvessels in tissues implanted in the mouse abdomen[142]. Therefore, our results suggest that a similar process of guided vascularization can occur on the heart.

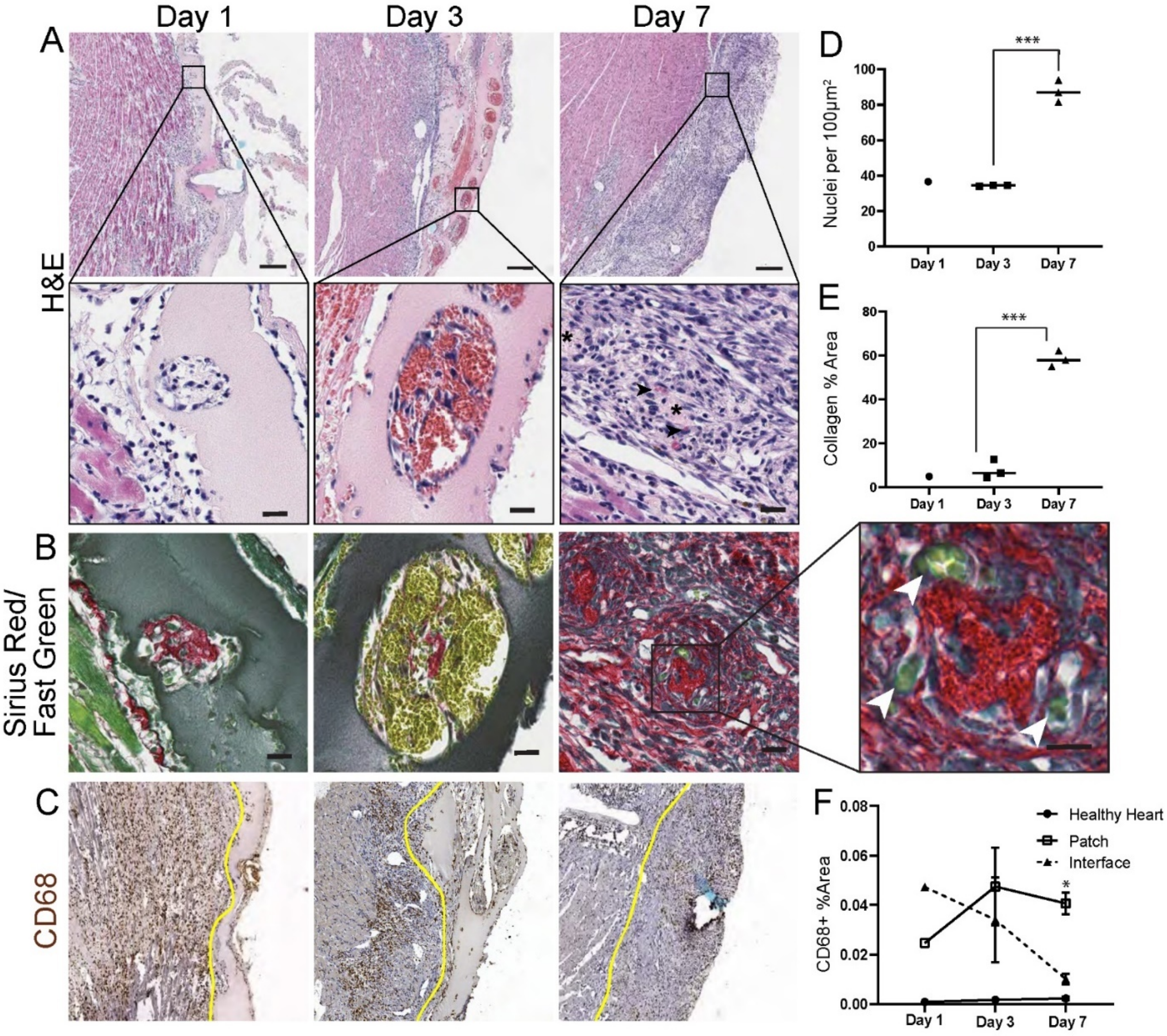

Figure 3.2 Cords patches become perfused at 3 days post-implantation. (A) H&E and (B) Sirius Red/Fast Green staining of cords patches explanted at 1, 3, and 7 days indicates pooling of blood around cords at day 3, followed by remodeling into micro-vessels (arrowheads, day 7) Scale bar = 20 µm, inset scale bar = 10 µm. (C) CD68+ cells are prevalent at all timepoints, remaining elevated in the patch at 7 days. Yellow line indicates patch boundary. Scale bar = 100 µm. (D) Hematoxylin positive nuclei within patch per 100 µm. (***$p < 0.001$). (E) Quantification of collagen area from Sirius Red stain. (***$p < 0.001$). (F) Quantification of CD68+ area (*$p<0.05$). Error bars indicate S.E.M. n=3 (day 3, day 7) n=1 (day 1).

In addition to revealing early infiltration of blood associated with cords, H&E staining showed a significant increase in density of hematoxylin positive nuclei within the patch between 3 and 7 days, suggestive of an inflammatory host response (Fig 3.2D). Correspondingly, the lightly eosin-positive fibrin identifiable at day 1 and day 3 appeared to be largely absent by day 7 (Fig 3.2A). To further characterize the apparent immune response, we immunostained for CD68, a macrophage marker. At day 1, we found marked infiltration of CD68+ cells at the patch periphery and extending several hundred microns into the heart tissue underlying the patch (Fig 3.2C). At the day 3 and day 7 timepoints we continued to observe CD68+ cells at the patch-heart interface and increased infiltration of CD68+ cells within patch boundaries. To better understand these trends, we quantified CD68+ area within the patch, in the heart-patch interface, and in tissue from a presumably healthy unperturbed area of the heart (Fig 3.2F). As expected, only rare CD68+ cells were observed within the distant healthy heart at all timepoints. Within the patch-heart interface, defined as the 300 μm underlying the patch, CD68+ area was initially elevated but was not significantly higher than healthy heart at 7 days. In contrast, CD68+ area within the patch remained elevated at levels significantly higher than healthy heart at 7 days.

To characterize the composition of the patch at 7 days, we stained for collagen with Sirius Red and counterstained with Fast Green (Fig 3.2B). At day 1 and day 3, we identified collagen at the center of the cords, consistent with our *in vitro* results. However, by day 7 collagen was identified both in the cords as well as throughout the patch, and the percent of patch area positive for Sirius Red had increased (Fig 3.2E). These results suggest that by day 7 the original fibrin scaffold had been degraded and replaced at least in part by a dense cellular milieu and collagen, likely largely derived from the host.

Next, we wanted to determine if the structures associated with the cords contained graft derived endothelial cells. Immunostaining for human CD31 identified human endothelium at 1, 3 and 7 days (Fig 3.3A). At day 1, the huCD31+ stained area was densely packed in cross sections of cords. By day 3, the staining indicated an expansion of the human endothelium to form large lumens, similar to previous observations of blood-filled lumen formation in mouse abdominal cords implants[142]. The area of huCD31+ cells as a percentage of patch area had decreased by 7 days, but the remaining cells had assembled as the interior lining of small lumens consistent with

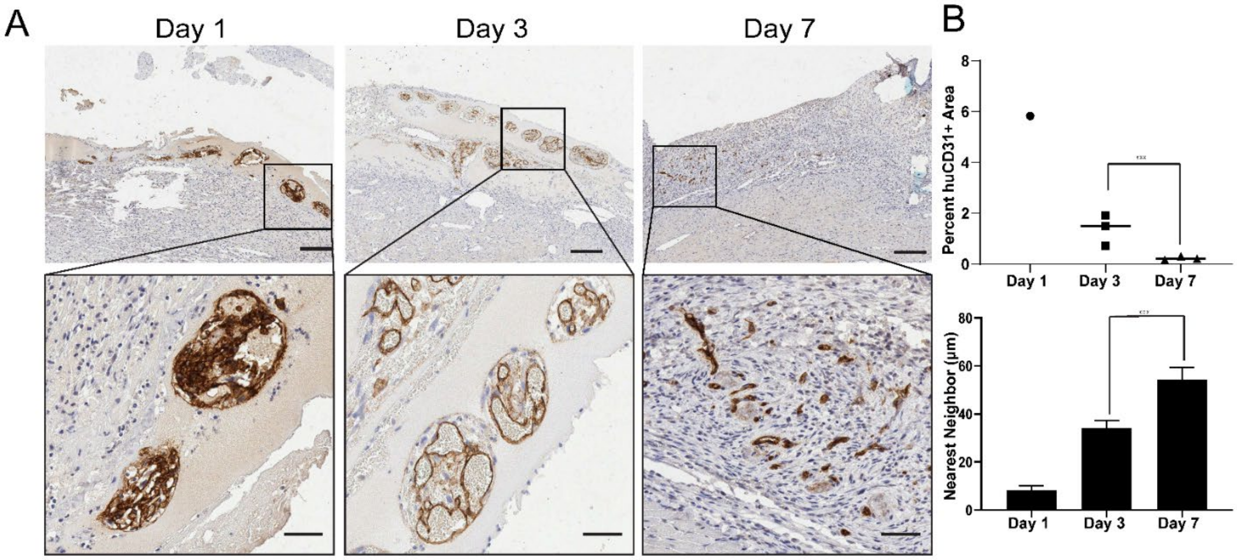

Figure 3.3 Human CD31+ cells form large lumens that reorganize into micro-vessels. (A) huCD31 staining of explants from 1, 3, and 7 days. Scale bar (top) = 200 µm. Scale bar (bottom) = 50 µm. (B) Quantification of huCD31 staining area as percent of patch over time (top). Nearest neighbor analysis of huCD31 staining at 1, 3, and 7 days (bottom). (***$p < 0.001$). n=1 for day 1, n=3 for day 3 and day 7. Error bars indicate S.E.M.

mature micro-vessel formation (Fig 3.3B). We noted the huCD31+ structures were no longer tightly associated with cords, as had been seen at 3 days. Instead, we found huCD31+ micro-vessels more diffusely arranged in the patch (Fig 3.3B, bottom).

3.4.3 Cords support formation of blood filled huCD31+ lumens

H&E and Sirius Red staining suggested the presence of blood-containing lumens associated with cords. Thus, we next sought to confirm the erythroid identity of these cells. Immunostaining for Hemoglobin A (marks rat red blood cells) confirmed the presence of blood within the graft at day 3 and day 7, but not at day 1 (Fig 3.4A). Co-staining for both huCD31 and HgbA identified lumens lined with human endothelial cells that contained rat blood at day 3 and day 7. At day 3, we noted ample blood present both within and proximal to the large huCD31+ lumens (Fig 3.4A). By day 7, we again found smaller huCD31+ vessels, some of which contained blood (Fig 3.4A). While there was not a significant change in total blood area within the patch between day 3 and day 7, we noticed a shift in distribution of both HgbA and huCD31 staining from highly clustered at 3 days to more disordered by 7 days (Fig 3.4B). To quantify this observation, we performed nearest-neighbor analysis of the huCD31 (Fig 3.3B) and HgbA stains (Fig 3.4B). This analysis confirmed a decrease in clustering of these markers between 3 and 7 days.

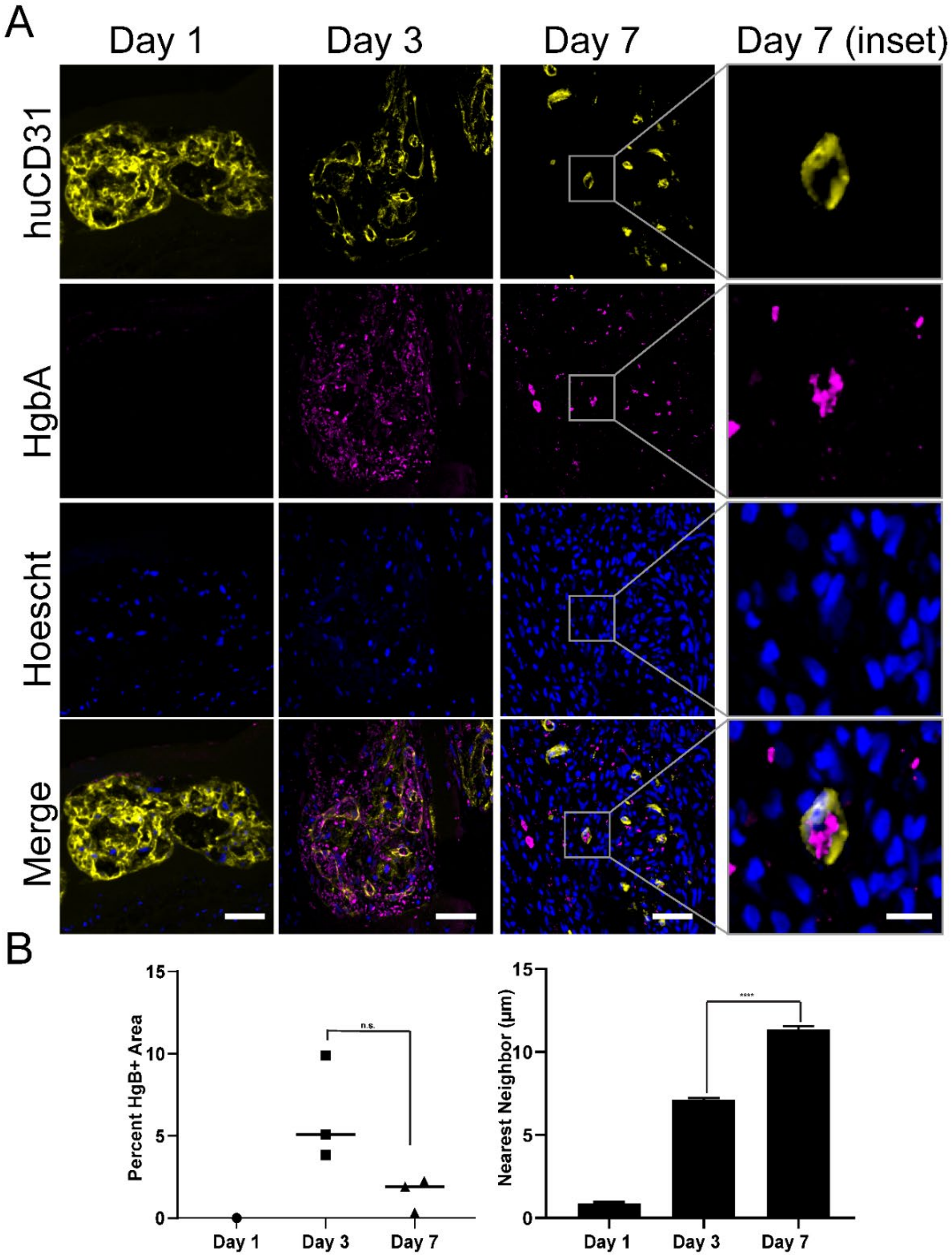

Figure 3.4 Graft-derived vessels are perfused with blood. (A) Co-staining for HgbA and huCD31 in explants from 1, 3, and 7 days. Scale bar = 50 µm. Inset scale bar = 10 µm. (B) Quantification of HgbA staining as percent of patch area and distance to nearest neighbor. (p***<0.001). n=1 for day 1, n=3 for day 3 and day 7. Error bars indicate S.E.M.

3.4.4 Co-engraftment of human myocardium and microvessels on the rat heart

As our ultimate goal is to induce vascularization of human engineered cardiac tissues, we sought to test whether cords could be integrated within a multicellular human myocardial patch. We adapted the basic cords patch fabrication protocol for this purpose by including human iPSC-cardiomyocytes, stromal cells (Normal Human Dermal Fibroblasts), and endothelial cells (HUVECs) within the fibrin bulk surrounding the patterned cords (Fig 3.5A). Staining of viable and non-viable cells within the cardio-cords patch confirmed that cells within the cords, and in the fibrin bulk, were viable after fabrication (Fig 3.5B). We then implanted patches on the surface of athymic rat hearts. Similar to the 7 day timepoint in previous experiments, we identified a collagen rich patch overlying the implant site (Fig 3.5C). As we had found in our previous studies, H&E staining confirmed the presence of micro-vessels throughout the patch area (Fig 3.5C, right). However, unlike the grafts containing only cords, the Sirius Red/Fast Green staining of cardio-cord grafts revealed a heterogenous staining pattern (Fig 3.5C, left). Against a background of dense Sirius-Red positive collagen, we identified several relatively large collagen-deficient, fast green positive islands. When we stained these sections for human myocardium using the marker β-myosin heavy chain, we were able to correlate these collagen-deficient islands with areas of engrafted cardiomyocytes (Fig 3.5D, left). We also identified human CD31 positive vessels, indicating a graft contribution to the vasculature (Fig 3.5D, right).

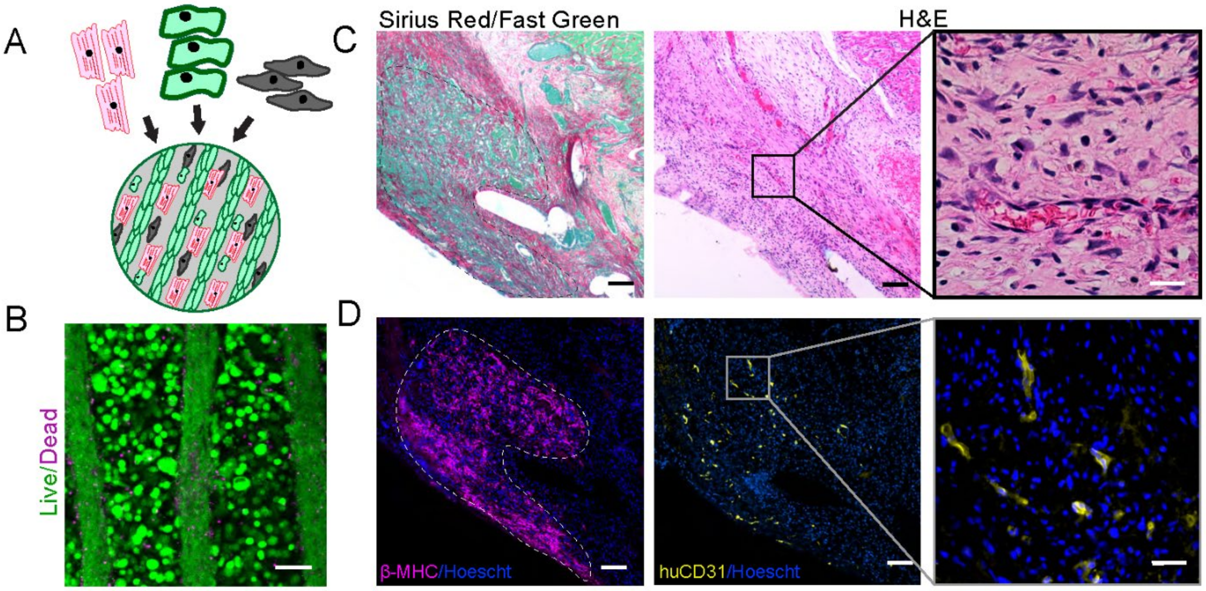

Figure 3.5 Cords-containing cardiac patch engrafts on rat heart. (A) Schematic showing composition of cardiac patch and (B) live/dead staining of patch at implantation, scale bar = 50 μm. (C) Sirius Red staining of patch at day 10 (left), and H&E staining of patch at day 10, inset shows microvessels (right). (D) Immunostaining of human graft (β-MHC) and endothelial cells (huCD31). Scale bar = 50 μm. Scale bar (inset) = 10 μm.

Although traditional tissue sectioning and histological imaging allowed us to identify human endothelial cells in patch sections, these methods did not provide information as to whether these cells reside within interconnected vascular networks that are patent and perfusable. To first better understand the 3D structure of patch derived vasculature, as well as the contribution of human *vs*. rat vessels after 7 days of implantation, we turned to emerging 3D tissue 'clearing' and visualization methods. First, we Langendorff perfused hearts with rodent specific (LEL) lectins. Next, we immunostained the intact hearts with a human-specific CD31 antibody. Samples were cleared with clearing-enhanced 3D microscopy (Ce3D)[162] and imaged to obtain a 200 μm thick z-stack through the patch (Fig 3.6A). We identified interconnected networks of human derived endothelial cells without obvious ‘cords’ patterning, as well as sparse rodent vessels, within the patches at 7 days post implantation. To improve the signal to noise ratio, images were segmented into stained and unstained regions using the machine learning based image analysis tool Ilastik[168]. Processed data revealed the boundary between patch and healthy heart to be approximately 150 µm from the patch surface. Quantification of human and rat contributions to the vessel network revealed primarily huCD31+ vessels within the first 100 µm from the patch surface (Fig 3.6B). A transition zone with both human and rat contributions was evident from approximately 100 µm to 150 µm from the surface, while rodent vessels from the rat heart predominated deeper than 150 µm. Therefore, vessels within the patch itself appeared to be primarily human derived, with some rat contribution deeper in the patch.

Next, we sought to determine whether the vessels within the patch were patent and perfusable. To do this, we used the optical coherence tomography (OCT)-based technique of optical microangiography (OMAG)[163], which provides information on both microvascular tissue structure and velocimetry. Imaging of patches at 7 days post implantation confirmed flow in the patch with a network of irregular microvessels near the surface of the tissue (Fig 3.6C). We also noted some regions of leakiness in the patch-heart interface. Together, these results demonstrate that patches contain interconnected networks of human endothelial cells and contain perfusable vessels at 7-days post implantation.

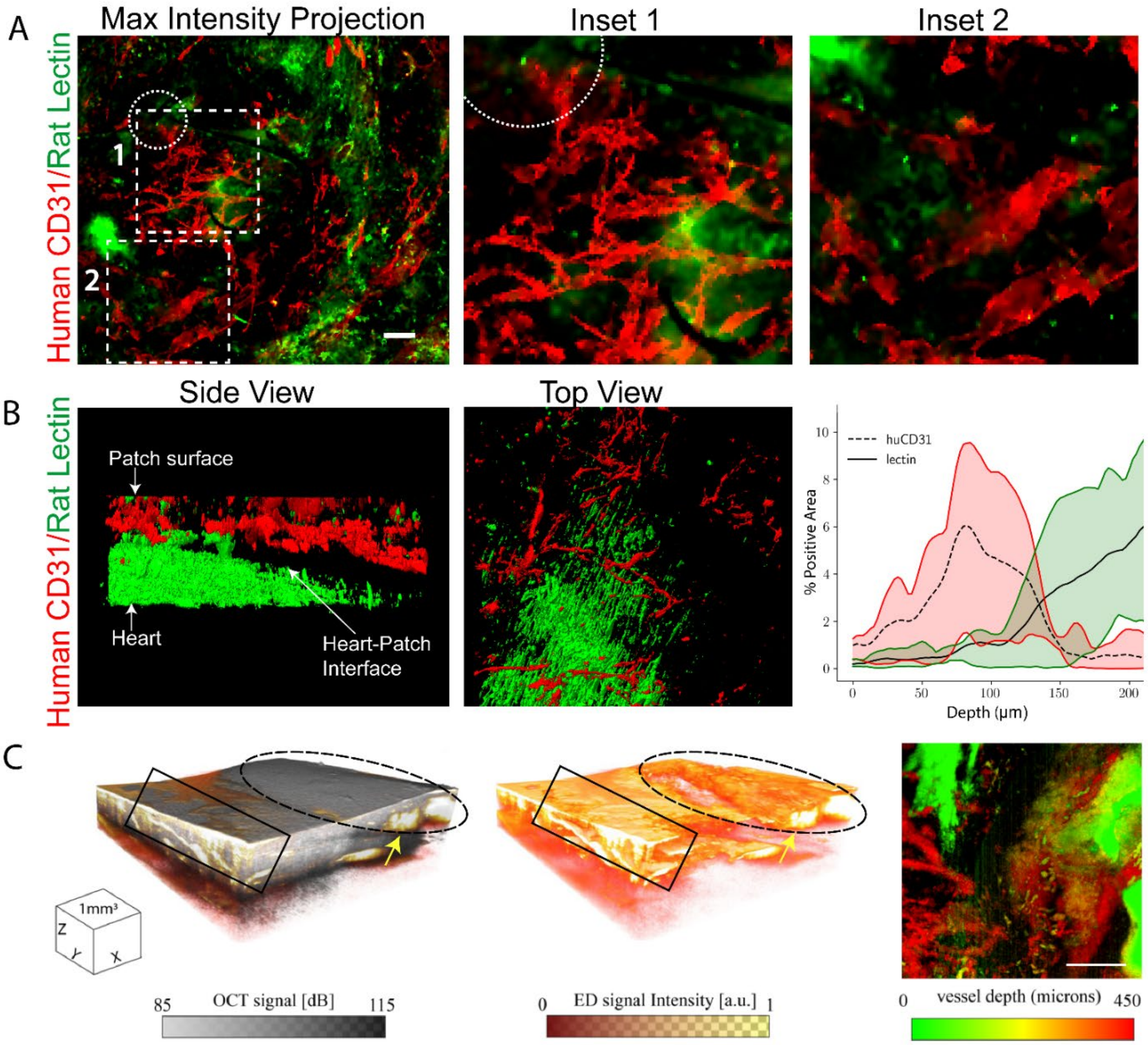

Figure 3.6 Lectin perfusion and optical micro-angiography (A). Maximum intensity projection of 200 µm z-stack of rat vessels stained with rodent specific lectin (LEL, green) and human vessels stained with an antibody for human CD31 (red). Dotted circle indicates location of suture. Scale bar = 100 µm. (B) 3D visualization of segmented data from rodent specific lectin (green) and human CD31 (red) staining. Quantification of area positively stained for human (huCD31) or rat (lectin) vessels in the patch region, range indicated by shaded region n=3. (C) 3D cube of OCT structural information overlaid with eigen decomposition (ED)-based OMAG signal showing flow through a network of irregular micro-vessels (arrow) in the patch region (dashed ellipse). 3D cube of ED-based OMAG signal showing only flow (middle panel). Intralipid leakage (box) at

the patch boundary can clearly be seen in the OMAG. En-face OMAG MIP image (right) of the vasculature (scale bar = 1mm). Deeper vessels (red) can be seen connected to surface vasculature.

3.5 DISCUSSION

Inefficient vascularization of engineered tissues remains a barrier to clinical translation. While early studies demonstrated that randomly seeded endothelial cells within engineered tissues can form rudimentary vascular networks, these networks are often transient and prone to failure[111,171]. Multiple studies have now shown that geometric patterning of vascular networks in engineered tissues leads to improved vascularization[70,142,171]. In this study, we have demonstrated that a bio-artificial tissue containing pre-formed “cords” of endothelial cells forms graft-derived microvessels containing blood when implanted on the supra-epicardial surface of the rat heart. At day 3, we noted robust patterning of nascent vessels. The large irregular lumens of these human CD31+ neovessels were filled with blood and appeared in tight association with patterned cords, which we identified by their Sirius-Red positive collagen cores. This initial process of cord-driven vascularization thus appeared morphologically similar to the process reported in mouse abdominal cords implants[142].

In previous studies of EC cords, these initial large lumens remodel to form an array of host-graft chimeric micro-vessels tightly clustered around the cords by 7 days post implantation. Interestingly, although we did find capillary to arteriole sized microvessels throughout our patch at 7 days, these vessels were not closely associated with cords. These results suggest that in the context of the rat heart, cords induce transient patterned vessel formation at 3 days, rather than persistent patterning as has been reported in the mouse abdomen[142]. Although we did not observe persistent patterning, we confirmed that vessels within the patch were perfusable at 7 days post-implantation.

This progressive loss of patterning corresponded with what appeared to be a robust inflammatory response. Interestingly, others have noted a heightened inflammatory response to supra-epicardial implants compared to implants in other locations[172,173]. Studies using other methods to pattern vascular networks have also observed loss of vascular patterning geometry after implantation on the heart[70]. Together, these data lead us to suggest that increased inflammation in response to implantation on the heart may cause patch degradation, collagen deposition, and loss of patterning. Despite this change in patch composition, we found large dense human cardiac grafts in patches containing endothelial cords, suggesting that the inflammatory environment still allowed engraftment. In addition, the areas of engrafted cardiomyocytes had notably less collagen deposition than surrounding areas devoid of cardiomyocytes. We note that the experiments here differ from previously published work on cords-containing tissues not only in implant location (abdominal vs. supra-epicardial), but also in host species (mouse vs. rat). Therefore, although we suspect increased inflammation associated with cardiac implant site is driving the observed differences, species-specific effects could provide an additive or alternative explanation. Future studies will need to determine whether vascular patterning is functionally advantageous in the context of the heart, compared to unorganized vascular networks. Perhaps more interesting will be investigation of the role of macrophages in vascular patterning and cardiac repair. As the recent work of work from the Molkentin laboratory indicates, an acute macrophage predominant response to cellular therapies in the context of the heart may in fact be critical for the success of these therapies.[174]

Together, our studies demonstrate the ability to transiently guide vascular patterning within bioartificial tissues engrafted on rat hearts. We speculate that inflammation leads to loss of scaffold architecture and rapid remodeling of the engineered construct in the heart compared to other implant locations. Concerningly, the problem of inflammation is likely to be exacerbated for injured hearts, where a wound healing response is already active. Thus, further characterization, and ultimately attenuation of host response may be critical for the field of cardiac tissue engineering[175].

CHAPTER 4. ENGINEERED TISSUE VASCULARIZATION AND ENGRAFTMENT DEPENDS ON HOST MODEL

4.1 ABSTRACT

Developing vascular networks that integrate with the host circulation and support cells engrafted within engineered tissues remains a key challenge in tissue engineering. Most previous work in this field has focused on developing new methods to build human vascular networks within engineered tissues prior to their implant *in vivo*, with substantively less attention paid to the role of the host in tissue vascularization and engraftment. Here, we assessed the role that different host animal models and anatomic implant locations play in vascularization and cardiomyocyte survival within engineered tissues. We found major differences in the formation of graft-derived blood vessels and survival of cardiomyocytes after implantation of identical tissues in immunodeficient athymic nude mice *versus* rats. Athymic mice supported robust guided vascularization of human microvessels carrying host blood but relatively sparse cardiac grafts within engineered tissues, regardless of implant site. Conversely, athymic rats produced substantive inflammatory changes that degraded grafts (abdomen) or disrupted vascular patterning (heart). Despite disrupted vascular patterning, athymic rats supported 30-fold larger human cardiomyocyte grafts compared to athymic mice. This work demonstrates the critical importance of the host for vascularization and engraftment of engineered tissues, which has broad translational implications across regenerative medicine.

4.2 INTRODUCTION

The need for transplantable organs far outpaces the number of available donor organs. As this discrepancy grows, an increasing number of patients on organ transplant waiting lists will die awaiting an organ[152]. Tissue engineering could address this problem by generating an alternative source of healthy human tissue for those unable to access donor organs. However, without a vasculature engineered tissues are limited in thickness by the diffusion limit of oxygen (100-200μm)[159,176,177]. Thus, vascularization is required to replicate the tissue thickness and complexity of commonly transplanted organs such as liver, lung, or heart.

Major progress towards vascularizing engineered tissues arose from the discovery that endothelial cells have the capacity to self-assemble into microvessel-like networks *in vivo*. These early experiments found that when endothelial cells were encapsulated in natural (fibronectin/collagen)[92] or synthetic (PLGA/PLLA)[93] hydrogel scaffolds and implanted in immunodeficient mice, they formed tubular networks that connected (anastomosed) to host circulation and contained host blood. Later studies further showed that including both endothelial and stromal cells within engineered tissues enhanced the vascular self-assembly process, leading to the formation of perfused, vascular networks that were at least in part derived from the grafted cells[27,94].

Despite this progress in leveraging cooperation between the graft and host for tissue vascularization, randomly self-assembled networks exhibited irregular vessel architecture, susceptibility to early thrombosis[110,111], and a delay between implantation and perfusion during which sensitive cells are deprived of oxygen. To address these limitations, we and others have developed methods to exert additional control over vascular architecture within the engineered tissue[65,142]. We developed a method to pattern endothelial cells and collagen into arrays of parallel channels and then encapsulate the resultant “endothelial cords” within engineered tissues[65,142]. Upon implantation in athymic mice, these endothelial cords act as “railroad tracks” that guide the formation of chimeric host-graft vessels that became anastomosed with the host circulation. Importantly, inclusion of patterned vascular networks improved the survival of functional hepatocytes within engineered liver tissue over randomly organized networks[142]. Due to this early success, we then sought to extend our approach for guided vascularization for cardiac tissue engineering, by implanting engineered tissues with endothelial cords on athymic rat hearts[151]. We were surprised to find robust inflammation and no evidence of patterned vessels after tissue implantation[151]. This result led us to hypothesize that different host models (here, animal models) and anatomic implant locations play underappreciated roles in the vascularization of human engineered tissues upon their implantation *in vivo*.

Here, we test this hypothesis and report divergent responses in vascularization and cardiomyocyte engraftment of engineered tissues after their implantation in athymic mice *versus* athymic rats. These results suggest that guided vascularization and cardiomyocyte survival are supported by different host factors, which vary across animal models. This work draws attention to the critical and often overlooked role that host factors play in affecting vascular integration and engraftment of engineered tissues.

4.3 METHODS

4.3.1 Cell culture and fabrication of cords patches:

Human Umbilical Vein Endothelial Cells (Lonza, P2-P4) were cultured in EGM-2 media (Lonza) on tissue culture treated poly(styrene). Mouse mesenchymal cells CH310t1/2 (ATCC, P5-P7) were cultured in low glucose Dulbecco's Modified Eagle's Medium (DMEM) supplemented with 10% v/v fetal bovine serum (FBS, BioWest). Normal Human Dermal Fibroblasts (Lonza, P5-P7) were cultured in DMEM supplemented with 10% FBS. Media was replaced every 48 hours and cells were passaged or used for experiments at 80% confluence. Patches containing endothelial cords were fabricated as has been previously described[142]. Briefly, HUVECs and CH310t1/2 cells were resuspended in a 2.5% collagen solution and introduced into a PDMS mold containing channels 150µm wide. Excess collagen was aspirated from the mold leaving the cell/collagen mixture only in the channels. Collagen polymerization was achieved by incubating the filled molds at 37°C for 8 minutes. Following polymerization, molds were incubated with EGM-2 media at 37°C for 3 hours to allow cord formation. Cords were then removed from the mold by encapsulating in a 1:1 mixture of 20mg/mL fibrinogen (Sigma) and 2.5U/mL thrombin (Sigma) that was allowed to polymerize. Last, a 6mm biopsy punch was used to punch out patches for implantation. Patches were then kept on ice floating in sterile EBM-2 (no supplements) until implantation.

For all cardiac patches, hES-CMs were prepared for implantation with heat-shock[178] and a pro-survival cocktail[179]. 24 hours prior to implantation, cardiomyocytes were changed to RPMI/BSA/Ascorbic acid that had been pre-warmed to 42°C and plates were incubated for 30 minutes at 42°C. After 30-minute heat shock, media was changed to RBA supplemented with 100 ng/mL IGF-1 (Peprotech) and 200nM Cyclosporine A (Wako). The next day, 1 hour prior to trypsinization, media was changed to RBA supplemented with pro-survival cocktail (100ng/mL IGF-1, 200nM Cyclosporine A, 10μM ZVAD-FMK (Calbiochem), 50nM TAT-BH4 (Calbiochem), 50μM pinacidil monohydrate (Sigma)). Immediately before the cord encapsulation step, $2x10^6$ hCMs and $5x10^5$ NHDFs were collected for each cords mold. For groups with HUVECs in the bulk, $1x10^6$ HUVECs per mold were also mixed with hCMs and NHDFs. The pooled cells were then resuspended in 20mg/mL fibrinogen and mixed thoroughly in a 1:1 ratio with thrombin to encapsulate cells in the bulk surrounding the cords. After fabrication, patches containing cardiomyocytes were kept on ice floating in sterile EBM-2 supplemented with pro-survival cocktail supplements described above.

4.3.2 Maintenance and differentiation of pluripotent stem cells

Human PSCs (WTC-11 or H7, Coriell) were maintained with mTeSR-1 media (Stemcell Technology) on Matrigel (BD Biosciences). Directed differentiation to cardiomyocytes was achieved through modulation of the Wnt pathway using small molecules[160]. Briefly, on day 0 hPSCs were changed to mTesR with 1μM Chiron 99021 (Tocris). After 24 hours, media was changed to Roswell Park Memorial Institute (RPMI) 1640 media supplemented with B27 (minus insulin) containing 1μM Chiron 99021. 48 hours later, media was replaced with RPMI/B27(minus insulin) with 2μM Wnt-C59 (Fisher). After 48 hours, media was changed to the final cardio maintenance media, comprised of RPMI with B27 supplement containing insulin. Thereafter, media was replaced every 48 hours. Between day 14 and 21, lactate selection with DMEM (no glucose) supplemented with 4 mM sodium lactate was performed for 72 hours, after which cells were returned to cardio maintenance media (RPMI/B27)[161]. Cardiomyocytes were used for experiments either directly following differentiation or were frozen and thawed for later use.

4.3.3 In vivo implantation in mice and rats

For all mouse experiments, male athymic nude mice (Taconic, 8-10 weeks), were used. Male athymic nude Sprague-Dawley rats (Envigo, 150-220g) were used for rat studies. For supra-epicardial patch placement, anesthesia was induced with either 5% isoflurane (rats) or ketamine/xylazine (130 mg/kg Ketamine, 8.8 mg/kg Xylazine, mice) preceding orotracheal intubation. Rats were maintained on 2% isoflurane and mice were supplemented with 0.5% isoflurane. The chest was opened via left lateral thoracotomy and the pericardium was removed to expose the heart. For rats, two 6mm patches were affixed using 8-0 suture to the supra-epicardial surface. Due to their smaller heart size, mice received one 6mm patch similarly affixed with 8-0 suture. The chest was closed, and animals were provided analgesia for the first two post-operative days via subcutaneous injection of slow releasing buprenorphine (1mg/kg). For animals that received patches containing cardiomyocytes, daily injections of Cyclosporine A (5mg/kg) were administered beginning one day prior to implantation.

Mice receiving intra-peritoneal implants were induced with ketamine/xylazine and a midline abdominal incision through the skin and peritoneum was made approximately 2mm offset from midline. A single 6mm patch was affixed with 5-0 suture to the gonadal fat pad. The incision was closed, and analgesia was provided for two days via slow releasing buprenorphine. All animal procedures were approved by the University of Washington Institutional Animal Care and Use Committee (IACUC protocol #4388-02).

4.3.4 Tissue harvesting, processing, and 2D histology

Animals were sacrificed at the pre-determined endpoint for each experiment (3 or 7 days for mice, 10 days for rats). For mice receiving fluorescent lectins, 200µl of a 1:1 mix of Dylight-649 conjugated Lycopersicon Esculentum (Tomato) Lectin (1mg/mL, Vector Labs) and Dylight-649 conjugated Ulex Europaeus Lectin 1 (1mg/mL, Vector Labs) was introduced via intravenous injection and allowed to circulate for 10 minutes prior to sacrifice. Tissues were fixed with 4% paraformaldehyde solution for 48 hours and immediately used for whole tissue staining, clearing, and 3D imaging (see below), or progressively dehydrated for paraffin embedding. Paraffin blocks were sectioned at 5µm with a microtome and sections collected on charged slides. Hematoxylin and Eosin (Harris hematoxylin and Eosin Y, Sigma) was used to visualize tissue morphometry. Collagen was identified with Picrosirius red (Direct Red 80, Sigma) using Fast Green (Sigma) as a counterstain. Prior to immunostaining, heat mediated antigen retrieval in pH 6.0 sodium citrate was performed. After blocking with 5% normal goat serum, primary antibodies were incubated at 4 degrees using antibodies against CD31 (1:20, Dako), TER-119 (1:100, BD Biosciences), α-Smooth Muscle Actin (1:100, abcam), and beta-myosin heavy chain (hybridoma supernatant, ATCC #CRL-2046, full strength) followed by species-appropriate secondary antibodies conjugated to Alexa Fluor 555 or Alexa Fluor 647. Nuclei were visualized with 1:500 hoescht 33342. Fluorescent images were acquired on a Nikon Eclipse Ti inverted microscope with either Photometrics CoolSNAP HQ2 camera for widefield images, or Yokogawa W1 spinning disk confocal head and Andor iXon Life EMCCD camera for confocal images. Images of H&E and

Sirius Red stains were obtained from whole slide scans acquired with an Aperio ScanScope AT2 digital whole slide scanner.

4.3.5 Clearing and 3D Imaging

Following fixation, whole tissues (gonadal fat pad or heart) were incubated for 6 hrs at 37°C in a blocking solution (0.1M Tris, 1% BSA, 1% Normal Donkey Serum, 0.3% triton x-100) followed by 24-hour incubation with 1:100 CD31/PECAM-1 DyLight 550 conjugated antibody (Clone: JC/70A, Novus) at 37°C on an orbital shaker. After staining, tissues were rendered optically transparent by clearing with the Clearing Enhanced 3D Microscopy (Ce3D) protocol at room temperature for 48hrs[162]. Cleared tissues were imaged with a Nikon Eclipse Ti inverted microscope with Yokogawa W1 spinning disk confocal head and Andor iXon Life EMCCD camera. After samples were imaged, cleared tissues were incubated with PBS overnight to remove clearing agents. Tissues were then processed for paraffin embedding and 2D histology as described above. 3D datasets were visualized with IMARIS 3D visualization and analysis software (Oxford Instruments).

4.3.6 Quantitative Tissue Morphometry

For all analysis, patch area was defined as the region between the surface of the host tissue (fat or cardiac) and the edge of the patch. Quantification of graft size (β-MHC) was accomplished using FIJI by applying a uniform threshold across images and measuring positive area[180]. All other stains (TER-119, huCD31, hoescht, H&E, and Sirius Red) were quantified by training the supervised machine learning image segmentation software ilastik to identify stained regions, and then measuring the area of stained regions using FIJI[168].

For vessel tracing and morphometry, a 250µm x 250µm x 250µm volume from the center of each patch was exported for analysis with the microvascular analysis suite Vesselucida (MBF biosciences). A semi-manual process was used for vessel tracing. First, small vessels were identified using the build in automatic tracing tool, which reliably identified vessels <10µm. Next, manual tracing was performed for all vessels not identified by automatic tracing. From these vessel tracings, the Vesselucida software generated data on vessel size for each network.

4.3.7 Statistical Analysis

Graphpad Prism software was used to complete all statistical analyses. For comparisons between two groups, an unpaired student t-test was performed. For analyses in which more than two groups were compared, a one-way ANOVA with Tukey's HSD as post-hoc test was used for data with equal variance, or Welch's Anova with Dunnett's T3 multiple comparison test was applied for data with unequal variance. Error bars are reported as SD.

4.4 RESULTS

4.4.1 Patches with endothelial "cords" retain patterning and anastomose with host circulation in the mouse abdomen and heart

We previously showed that patterning endothelial cells and collagen into cord-like structures within fibrin-based engineered tissues facilitates the guided formation of patterned, chimeric host-graft vessels upon their intraperitoneal (IP) implantation in the abdomen of athymic mice[142]. Yet paradoxically, we also showed recently that such engineered tissues are rapidly degraded and do not retain vessel patterning after 7 days of implantation on the heart of athymic rats[151]. We first hypothesized that differences in host response across anatomic locations of the implanted tissue, in this case between the heart and the abdomen, might explain these results.

To methodically test this hypothesis here, we suspended endothelial cells (HUVECs) and stromal cells in collagen within a PDMS mold with parallel channels to form “endothelial cords”, then encapsulated these cords within fibrin to create engineered tissues, as we have done before[142]. We suspended endothelial cells (HUVECs) and stromal cells in collagen within a PDMS mold with parallel channels to form “endothelial cords”, then encapsulated these cords within fibrin to create engineered tissues, as we have done before[142]. We then randomly allocated these tissues into two groups and sutured the tissues from each group onto either the intraperitoneal (IP) gonadal fat pad or on the epicardial surface of the heart in athymic nude mice (Fig 4.1a). These engineered tissues were explanted at either 3 or 7 days post implantation for histological analyses. Upon gross examination at explanted tissues, we identified intact engineered tissues with minimal adhesions at 3- and 7-day timepoints at each anatomic implant location (Fig 4.1a). Furthermore, Hematoxylin and Eosin (H&E) and Sirius Red staining of sectioned explanted tissues revealed regularly spaced clusters of cells in a pattern reflecting cord cross-sectional geometry from both locations at 3 and 7 days (Fig 4.2, Fig 4.1b). Within these clusters, these stains identified a collagen core that became surrounded by blood-containing lumens by 7 days (Fig 4.1b). We next assessed inflammation by looking for nuclear infiltration and collagen deposition within the explanted engineered tissues. Whereas hematoxylin-positive nuclei were present at the grafted tissue boundary, nuclear infiltration did not extend into the graft, suggesting that the inflammatory response was contained at the host-graft interface. Furthermore, all explanted tissues had an intact Eosin-positive fibrin matrix without interstitial collagen deposition (Fig 4.1b). Taken together, these results demonstrate a morphologic pattern of cord-associated lumen formation with minimal inflammation in both IP and epicardial implant locations in athymic nude mice.

To further explore the phenotype of cells in these structures, we performed immunostaining with a human specific anti-CD31 antibody (huCD31) and a mouse specific red blood cell marker (TER-119). This staining revealed that cords-associated lumens at both implant locations are lined with human endothelium and contain mouse red blood cells (RBCs) (Fig 4.1c). Additionally, this staining confirmed that cords geometry was retained in patches from either implant location, with huCD31+ cells found almost exclusively in distinct clusters of lumens spaced approximately 50-100μm apart (Fig 4.1c, arrows). Quantification of collagen, fibrin, cellular nuclei (hoescht), huCD31, and blood (TER-119) area showed no significant differences in patch architecture, inflammation, or vascularization between implant locations at 7 days (Fig 4.1d). Overall, our results demonstrate that guided vascularization[142] occurs at both IP and epicardial (heart) implant locations in athymic nude mice.

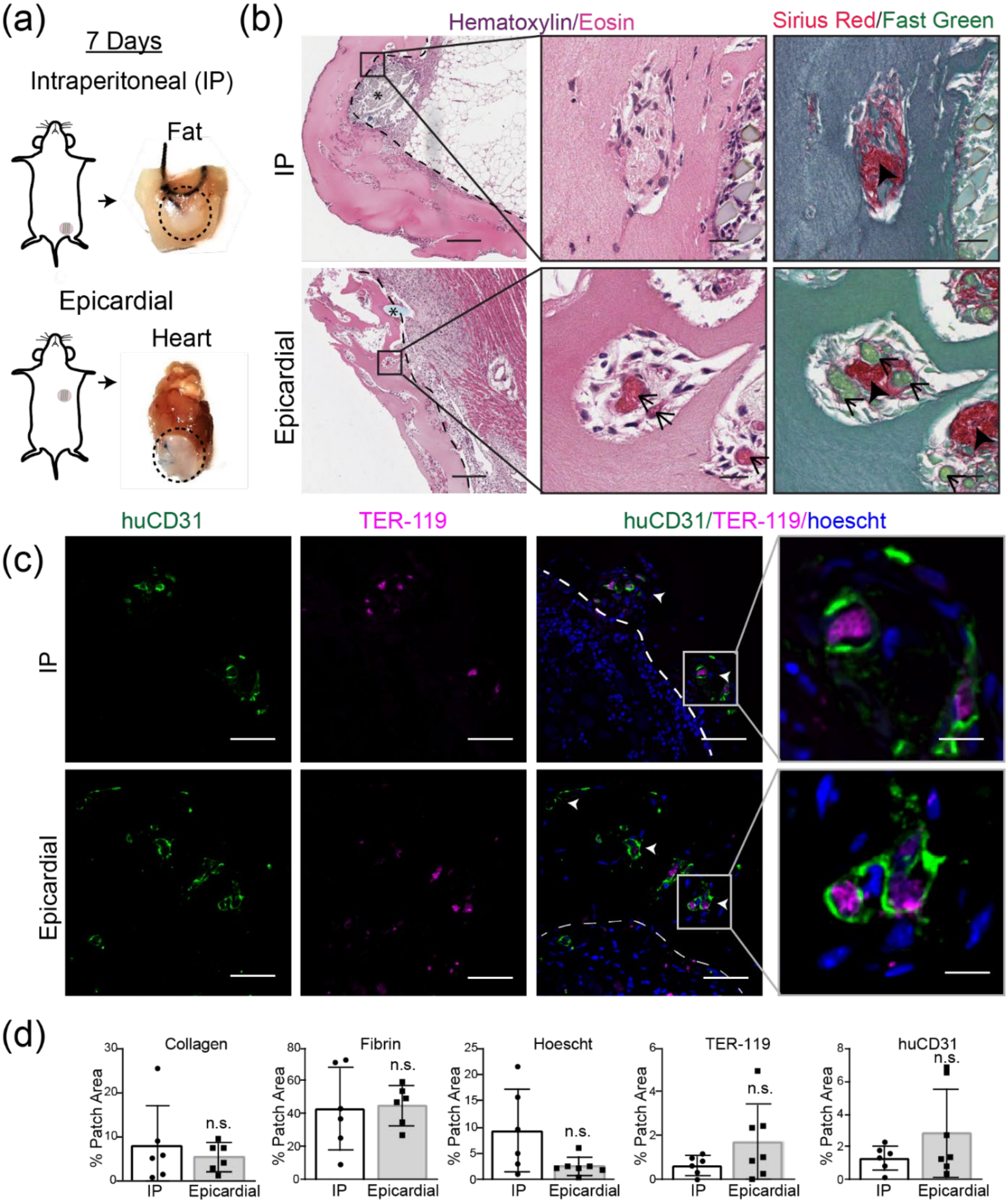

Figure 4.1 Guided vascularization occurs in Intra-peritoneal (IP) and epicardial implants in mice. (a) Explants from gonadal fat pad (IP) or epicardial (heart) locations have intact patches at 7 days (dotted lines). (b) H&E and Sirius Red/Fast Green stains of day 7

explants show cords-associated vessels in both IP and epicardial implants. Dashed line indicates host-graft boundary, asterisk marks suture. Insets: open arrows indicate blood pools, closed arrows mark collagen cords. Scale bar = 200μm (left). Inset scale bar = 20μm. Immunostaining (c) confirms regular clusters (white arrows) of graft-derived vessels (huCD31+) filled with mouse blood (TER-119+). Scale bar = 50μm. Inset scale bar=10μm. (d) Quantification of staining by percent patch area shows no difference between groups in collagen, fibrin, nuclei, blood (TER-119), or huCD31. Each point represents an individual animal. Error bars reported as S.D.

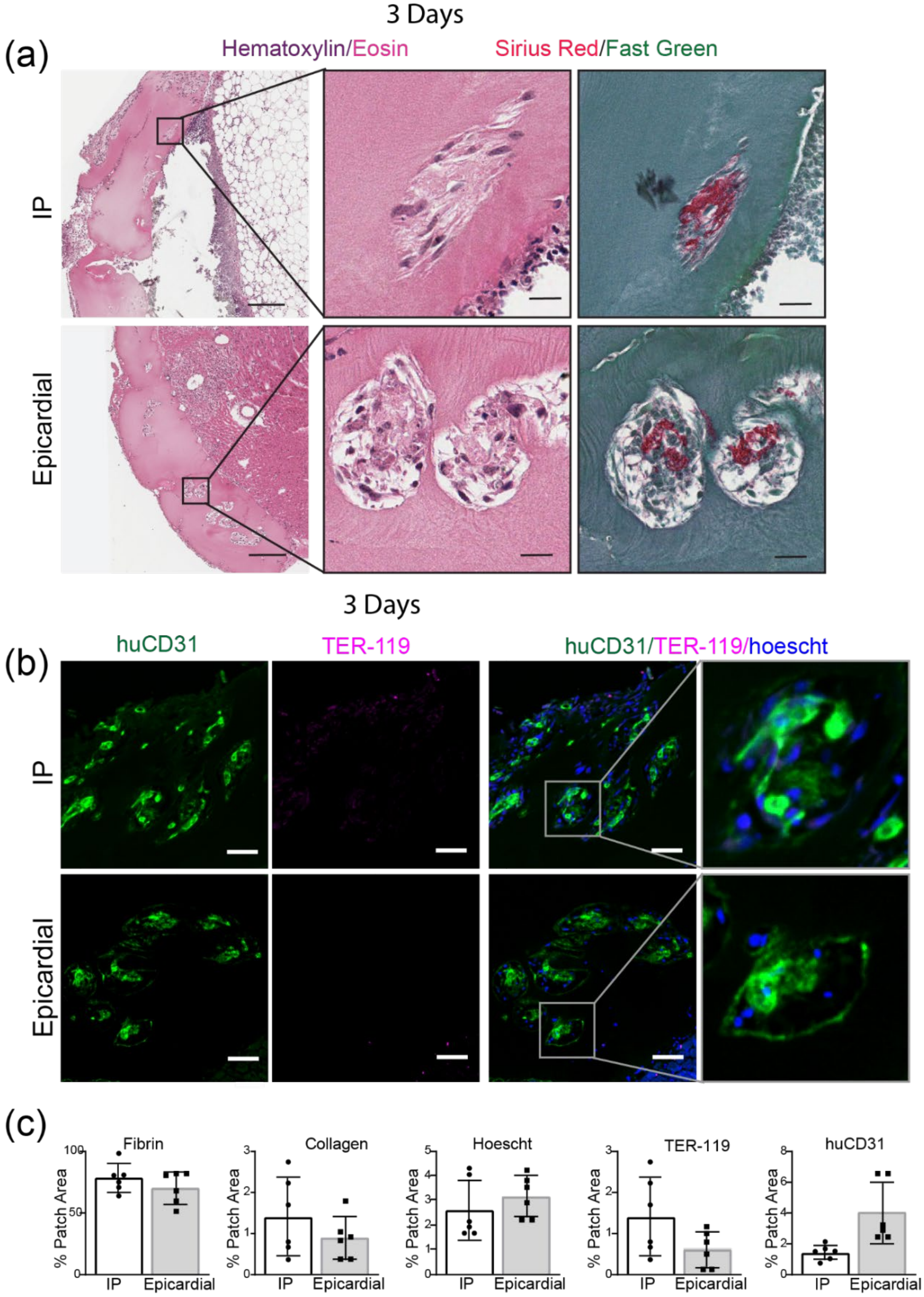

Figure 4.2 3-day epicardial and abdominal implants in mice. (a) H&E and Sirius Red/Fast Green stain of cords-containing fibrin patches 3 days post-implantation in

mice. Scale bar = 200μm. Inset scale bar = 20μm. (b) Immunostaining of 3-day patches with huCD31 (green), TER-119 (magenta), and hoescht (blue). Scale bar = 50μm. (c) Quantification of fibrin, collagen, hoescht, TER-119, and huCD31 reported as percent of patch area. Error bars show S.D.

4.4.2 Cords-containing cardiac patches in mice develop patterned vessels with increased lumen size

After we had confirmed that guided vascularization occurs in the mouse heart, we next sought to apply this technique for cardiac tissue containing not only vascular cells, but also human pluripotent stem cell-derived cardiomyocytes ("cardiomyocytes"). We fabricated engineered tissues containing randomly seeded cardiomyocytes along with three endothelial cell patterning compositions: 1) patterned EC cords as well as randomly seeded ECs in the bulk (cords + bulk), 2) ECs in cords only (cords), 3) randomly seeded ECs in the bulk only (bulk) (Fig 4.3a).

To compare vascularization between groups, we first used 2D histology to assess overall tissue structure and look for evidence of blood-vessels within the grafts. Hematoxylin and Eosin and Sirius Red stains suggested guided vascularization had occurred, with blood pools associated with collagen cords in both cords+bulk and cords-only groups (Fig 4.3b). Similar large blood consolidations were absent in patches lacking cords (Fig 4.3b). Patches from all groups remained intact with minimal collagen deposition or excessive inflammation, with no significant differences between groups (Fig 4.3c). To further compare graft-derived vessel morphology between groups, we co-stained for human endothelium (huCD31), mouse erythrocytes (TER-119), and the pericyte marker α-smooth muscle actin (Fig 4.3d). Compared to patches with only unpatterned ECs, we found that graft-derived endothelial cells in cords-containing groups more efficiently recruited blood (Fig 4.3c). We then assessed for the presence of α-SMA+ pericytes, which are a marker of mature microvessels[181]. We found the cords-associated vessels often had nearby α-SMA+ cells (Fig 4.3d). Additionally, some of these vessels had α-SMA+ cells partially or fully encircling the huCD31+ lumen, as would be expected in mature vessels (Fig 4.3d, inset). The increased efficiency of blood recruitment and the presence of vessel associated α-SMA+ cells suggest that guided vascularization could support stable vessel formation in the mouse heart.

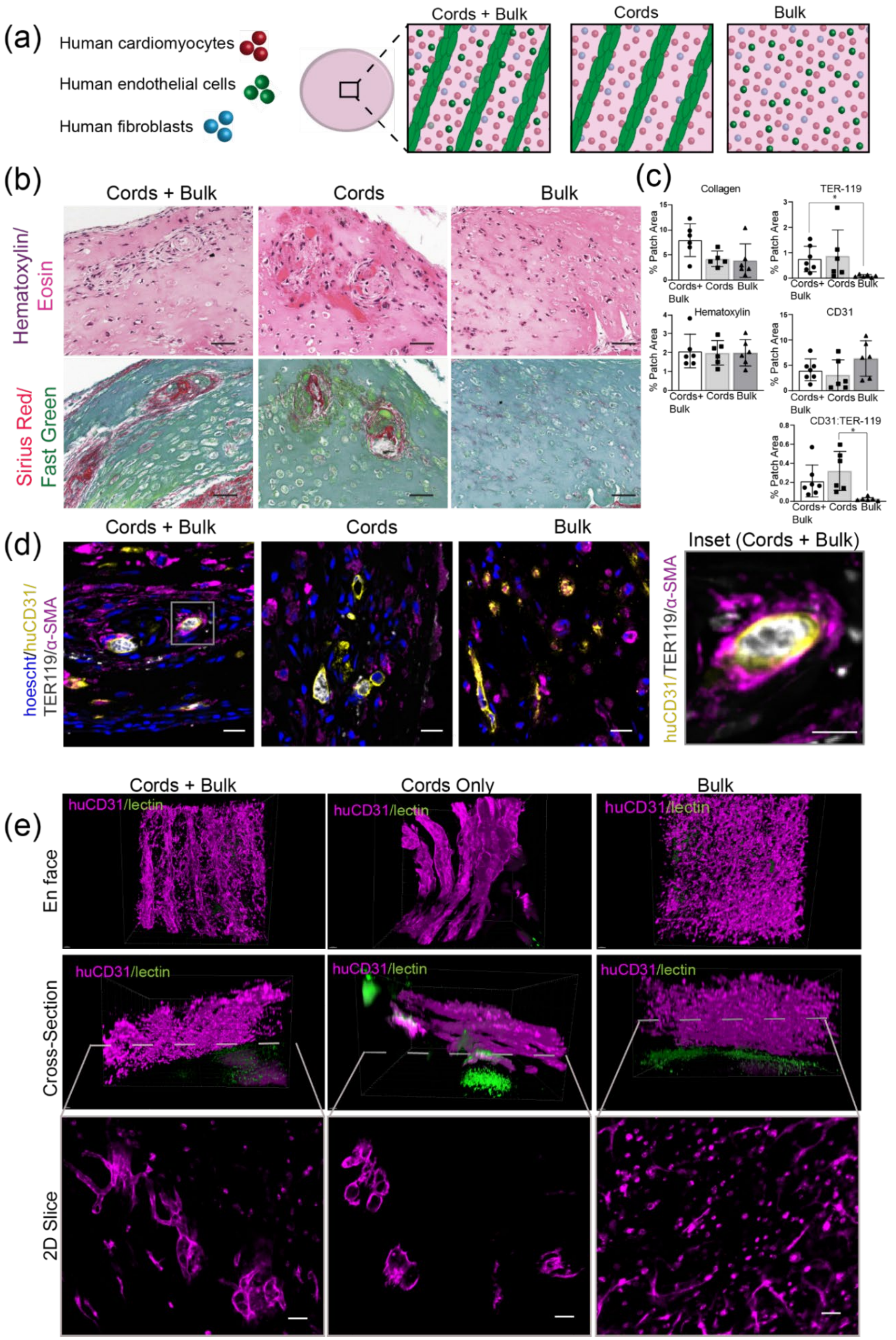
(a)
Human cardiomyocytes
Human endothelial cells
Human fibroblasts
Cords + Bulk
Cords
Bulk
(b)
Cords + Bulk
Cords
Bulk
Hematoxylin/ Eosin
Sirius Red/ Fast Green
(c)
Collagen
TER-119
Hematoxylin
CD31
CD31:TER-119
% Patch Area
Cords+ Bulk
Cords
Bulk
*
(d)
Cords + Bulk
Cords
Bulk
Inset (Cords + Bulk)
hoescht/huCD31/ TER119/α-SMA
huCD31/TER119/α-SMA
(e)
Cords + Bulk
Cords Only
Bulk
En face
Cross-Section
2D Slice
huCD31/lectin

Figure 4.3 EC cords guide vascularization of engineered cardiac tissues in the athymic mouse heart (a) Human cardiomyocytes, ECs, and stromal cells were used to create cardiac patches with different tissue geometries. (b) Hematoxylin & Eosin and Sirius Red demonstrate cords-associated blood pools in patches containing EC cords. Scale bar = 50μm (c) Quantification of collagen, nuclei, huCD31, TER-119, and huCD31:TER-119 between patches with different EC configurations. Error bars report S.D. (d) Patterned huCD31+ vessels are filled with blood (TER-119) and recruit α-SMA pericytes. Scale bar = 20μm. Inset scale bar = 10μm. (e) Top: 3D visualization of huCD31 (magenta) and intravenously circulated fluorescent lectins (UEA-1 and LEL, green). Bottom: single 2D slice taken from z-stack at level indicated by dashed line. Scale bar = 50μm.

While the clustered pattern of graft-derived vessels in the 2D staining data suggested that vessels retained cords geometry in mice, we wanted to better understand three-dimensional (3D) engineered vascular geometry on the surface of the heart. To do this, we stained whole tissues for human endothelium (huCD31) and imaged the cleared samples with confocal microscopy. We also visualized perfused vessels using fluorescent lectin that had been introduced intravenously prior to harvest. In both cords-containing groups, we identified a parallel array of huCD31+ vessels (Fig 4.3e). Cross-sections of these cords revealed hollow 20-40μm lumens forming “trunks” aligned with the axis of each “cord”, and smaller vessels branching orthogonally from these larger trunks. No patterning was evident in the bulk-only patches. Instead, the bulk-only tissues had small vessel-like structures scattered throughout and many huCD31+ cells remained as isolated cells not incorporated into vessels (Fig 4.3e). The group containing both cords and HUVECs in the bulk had features of both the cords and bulk-only groups, with larger vessels in the cords and smaller vessels and unincorporated huCD31+ cells throughout. To quantify the observed differences in vessel size between cords-associated vessels and those derived from randomly seeded HUVECs, we used Vesselucida software to generate tracings of vessels from each engineered tissue (Fig 4.4a). Analysis of these tracings showed that vessels in the bulk-only group were significantly smaller than those in the cords-containing groups, with an average of 86% of vessels in bulk-only patches having a diameter <10μm and less than 1% having diameter >20μm (Fig 4.4b). The cords-associated vessels were significantly larger, with an average diameter close to 20μm (Fib 4.4b). In the tissues with both cords and bulk HUVECs, vessels in the cords (black) more closely matched the cords-only group, while vessels in the bulk (gray) were similar in size to those in the bulk-only cohort (Fig 4.4c). While 2D immunostaining identified blood within graft-derived lumens, indicating anastomosis with the host circulation, we very rarely observed lectin+ vessels in the patches in any group (Fig 4.3e), suggesting that flow in patches was too slow to be detected in the lectin circulation time. Taken together, these data indicate that in the athymic mouse heart EC cords guide the formation of patterned blood-filled vessels with larger lumen sizes compared to vessels assembled from homogeneously seeded cells, albeit with circulation that remains lower than that of the host coronary vasculature. Thus, guiding vascularization with EC cords may be a viable strategy for cardiac tissue engineering applications in an appropriate host setting.

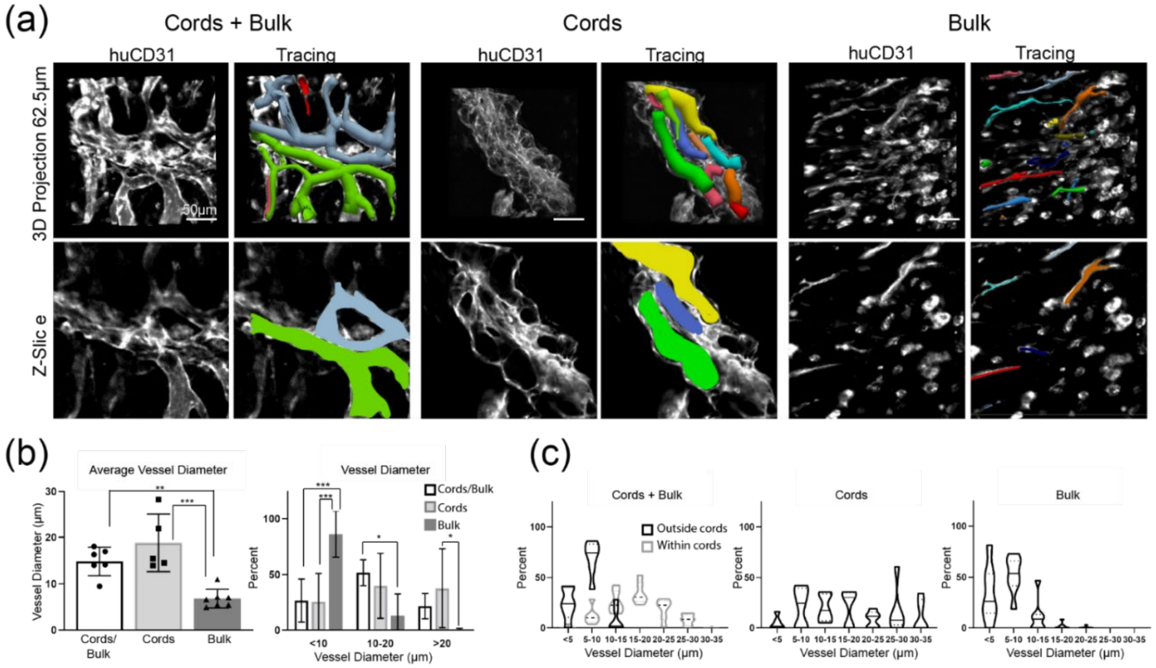

Figure 4.4 Vessel tracing and morphometric analysis. (a) Vesselucida software was used to trace all vessels within a 250µm^3 ROI taken from the center of each patch. (b) Quantification of vessel diameter from traced vessels. Error bars indicate S.D. (c) Vessels found outside cords (black) are smaller than those found within cords (grey).

4.4.3 Animal model differences in response to cords-containing human cardiac patches

From our studies of cords-containing cardiac tissues in mice, we saw that vascular patterning was retained, and furthermore that endothelial cords influence the organization and size of vessels formed *in vivo*. Yet we were surprised to find that despite vessel formation and anastomosis *in vivo*, the human cardiomyocyte grafts remained rather small and dispersed across all conditions (Fig 4.5). We found this particularly interesting since we and others have observed substantive cardiac grafts previously in other settings, such as in the athymic nude rat. Thus, we wanted to further explore the host response to grafts in athymic nude mice *versus* rats.

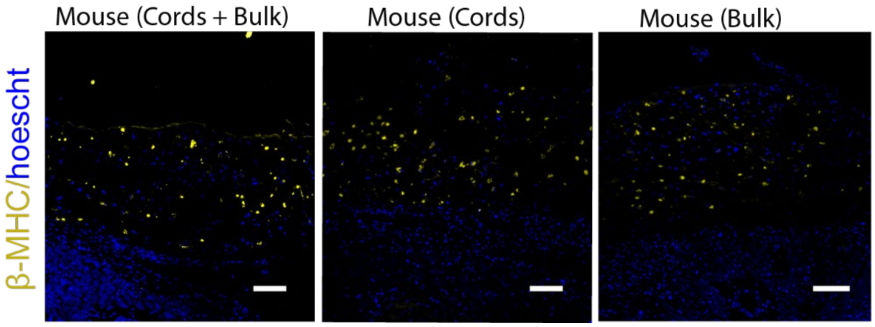

Figure 4.5 β-MHC+ cardiac grafts in mice remain sparse despite guided vascularization. Scale bar = 100μm.

As a first step, we performed an “implant location” study in athymic nude rats, as we had done in athymic nude mice (Fig 4.1). We implanted identical fibrin patches containing endothelial cords either in the abdomen (IP space) or the epicardial surface of athymic rats. Upon retrieval of the tissues from the IP location, we were able to identify the location of the implant by visualizing the suture but could not identify any of the engineered tissues in any of the animals, either by gross observation or upon histologic examination through the plane of the suture (Fig 4.6).

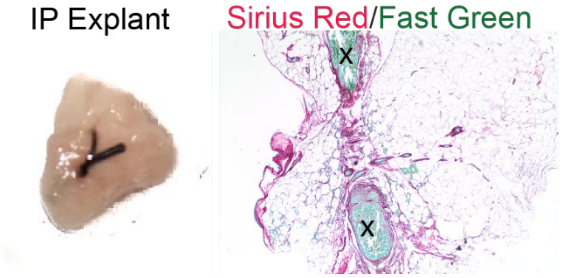

Figure 4.6 Fibrin tissues containing EC cords are obliterated in the athymic rat IP space at 7 days. Left: explanted gonadal fat with intact suture but no visible patch. Right: Sirius Red/Fast Green through the middle of the suture (suture = x) fails to reveal remaining fibrin.

Conversely, all epicardial implants were identified grossly at the time of explant and further histologically processed. Histological staining of the epicardial explants with Hematoxylin and Eosin and Sirius Red revealed an inflammatory reaction characterized by nuclear infiltration, collagen deposition, and minimal remaining fibrin matrix (Fig 4.7a), consistent with our previous findings[151]. Further immunostaining revealed numerous CD68+ macrophages throughout the tissue and concentrated around the perimeter of the remaining fibrin (Fig 4.7b), as well as microvessels lined with huCD31+ graft-derived endothelial cells scattered throughout the graft (Fig 4.7c). Further 3D huCD31 staining, clearing, and imaging of whole tissues (Fig 4.7d) demonstrated the presence of human vessel structures with diameters in the range of 5μm-10μm, with minimal architectural patterning (Fig 4.7d). Thus, athymic rats appeared to produce a robust inflammatory response that seemingly degrades engineered tissues in the IP space and disrupts vessel patterning in those implanted on the epicardial surface of the heart[151].

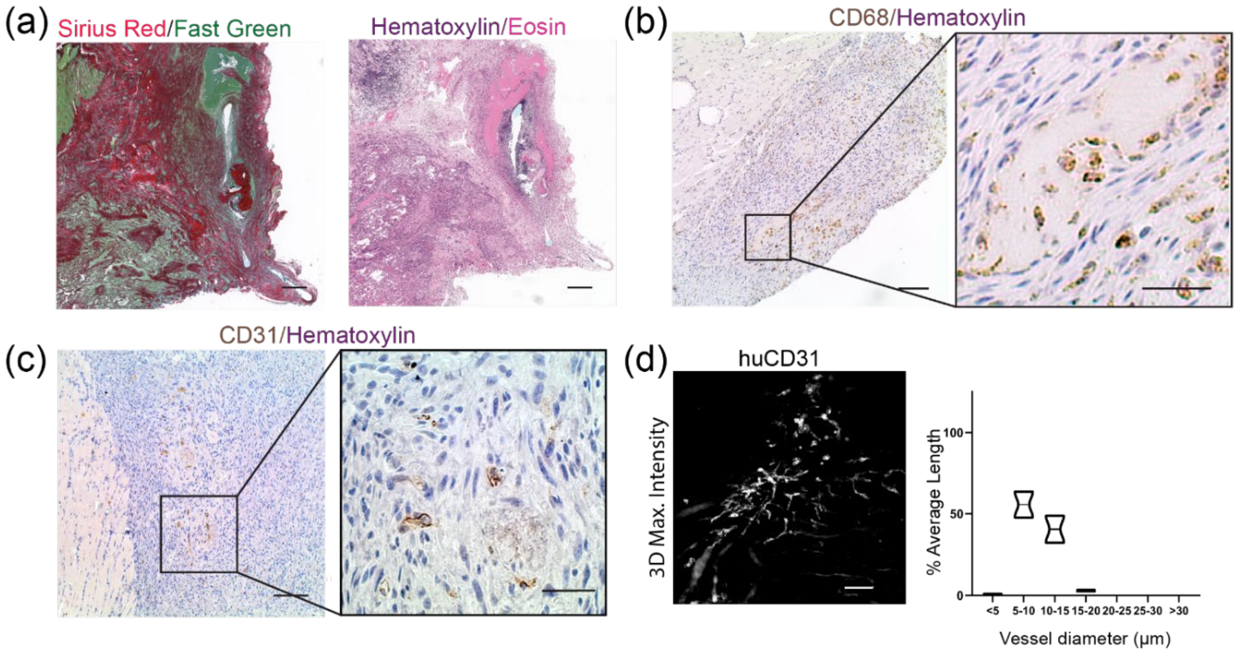

Figure 4.7 Fibrin patches with cords induce inflammation on the athymic rat heart. (a) Sirius Red staining reveals the fibrin matrix has been replaced by dense collagen (left). Hematoxylin & Eosin shows robust nuclear infiltration throughout the patch, with no evidence of patterned vessels (right). Scale bar = 100µm. (b) Immunostaining identifies numerous CD68+ macrophages clustered around the remaining fibrin (inset). Scale bar = 50µm, inset scale = 20µm. (c) Staining for huCD31 reveals sparse graft-derived vessels. Inset shows close view of a cord with occasional graft-derived vessels in the vicinity. Scale bar = 50µm, inset scale = 20µm (d) 3D projection of huCD31 staining from a cleared tissue (left). 3D stacks were used to generate vessel traces and quantify lumen size using Vesselucida software (right). Scale bar = 100µm.

We next directly compared engraftment of engineered cardiac tissues on the epicardial surface of athymic mouse or rat hearts. We fabricated cardiac tissues containing endothelial cells in both cords and the tissue bulk, as well as human cardiomyocytes. These tissues were then distributed for implant on the hearts of athymic rats or mice. Upon retrieval of the tissues, we found that the explanted tissues from mice had evidence of guided vascularization, with Hematoxylin and Eosin staining showing large blood-filled lumens in a linear pattern reminiscent of cord cross-sections and Sirius Red staining confirming these were associated with collagen cords, similar to our previous results (Fig 4.8a, 4.1b). In contrast, tissues recovered from rats had no evidence of cords-associated blood consolidations (Fig 4.8a). Instead, most of the tissue was replaced by a collagen matrix in rats, with >3-fold more collagen found in tissues in rats compared to those in in mice (Fig 4.8b). While little fibrin remained in rat explants, the tissues recovered from mice contained primarily Eosin-stained fibrin, with some collagen present at the graft-host boundary and within the cords (Fig 4.8a). We also noted substantively more Hematoxylin-positive nuclei, indicative of an inflammatory response, in the tissues recovered from athymic rats compared to mice (Fig 4.8a,b).

Finally, we performed immunostaining to identify human graft-derived endothelial cells and cardiomyocytes in explanted tissues from the two animal models. Immunostaining revealed that cords-containing patches in mice had distinct clusters of huCD31+ lumens that contained TER-119+ mouse blood, whereas the tissues explanted from rats had no discernible patterning of graft-derived cells (Fig 4.8c). To further assess human cardiomyocyte graft size within explanted tissues, we stained for human myocardium with β-MHC (Fig 4.8d). Interestingly, grafts explanted from athymic rats were ~30-fold larger grafts explanted from mice (Fig 4.8b). Morphologically, β-MHC cells in the tissue grafts explanted from rats were closely packed with larger cells that sometimes appeared elongated, while cells in the grafts in mice were isolated and small with a rounder, more punctate appearance (Fig 4,8d, inset). Thus, while vascular patterning was retained in mice but disrupted in rats, cardiomyocyte engraftment as measured by overall graft size was paradoxically superior in rats despite apparent inflammation. These surprising results indicate a major variable that has been previously overlooked by our field, by demonstrating that identical tissues, when implanted in different hosts, will yield vastly different engraftment results.

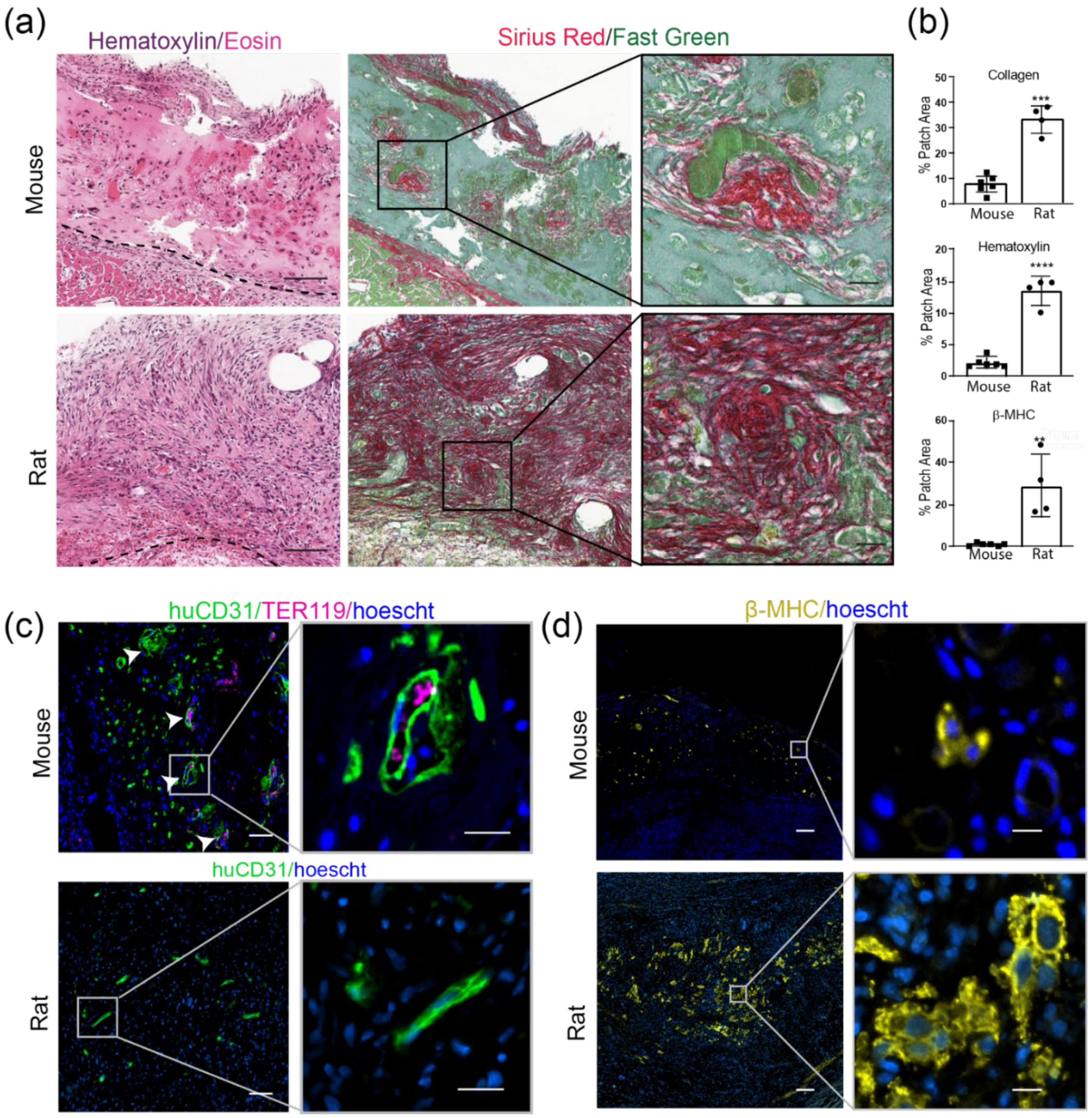

Fig. 4.8 Cords-containing cardiac patch induces patterned vasculature in mice, but robust inflammation in rat. (a) H&E and Sirius Red/Fast Green show hematoxylin-positive nuclear infiltrate and SR+ collagen in patches implanted in rats, but minimal inflammation in mice. Dashed line indicates host-graft boundary. Patches in mice have

blood pools associated with cords (inset). Scale bar = 100µm. Inset scale bar = 20µm. (b) Quantification of collagen, nuclei, and human myocardium as percent of patch area in rats and mice. Error bars report S.D. (c) In mice, huCD31 staining reveals cords-associated clusters of graft-derived vessels filled with TER-119+ blood (white arrows indicate cords). huCD31 staining in rats fails to recapitulate cords patterning. Scale bar = 50µm. Inset scale bar = 20µm (d) Human cardiac graft size is larger in rats than mice. Scale bar = 100µm. Inset scale bar = 10µm.

4.5 DISCUSSION

We previously demonstrated that endothelial cell “cords” encapsulated in a fibrin-based tissue guide the formation of host-perfused vessels along the axis of each cord in athymic mice[142]. However, when we attempted to replicate this strategy in a cardiac patch implanted in athymic rats, the cords led to only transient vessel patterning. In addition to loss of vessel patterning, we also observed a robust immune response leading to patch degradation and collagen deposition. Here, we meticulously assessed how host variables – anatomic implant location and animal model – differentially support guided vascularization and cardiac engraftment.

We first postulated that anatomic implant location may be the major variable at play in our studies, as others have reported a particularly robust immune response to biomaterials implanted in the epicardial environment compared to other anatomic locations[172,173]. For example, Kellar et. al implanted collagen discs epicardially in mice and found increased leukocyte recruitment, inflammatory cytokine expression, and matrix degradation compared with subcutaneous implants[173]. Similarly, ePTFE discs implanted epicardially in rats showed increased immune cell density compared with either subcutaneous or abdominal implants[172]. Interestingly, we found no differences in tissue morphology or vascularization between engineered tissues with EC “cords” implanted in either the IP space or on the heart in nude mice. We speculate that our failure to detect a difference between implant locations here could be explained by strain differences in immune response of athymic nude mice, as previous studies reporting increased inflammation in in epicardial implants have used immune-competent strains such as C56Bl/6 mice. The discrepancies between such studies thus may once again highlight the role for host factors and model systems as playing a role in tissue engineering outcomes.

Having found that athymic nude mice support guided vascularization in epicardial implants, we next sought to apply this strategy in the context of cardiac tissue engineering. By comparing engineered cardiac tissues with and without EC cords, we found that patches with EC cords more efficiently recruit host blood compared with unpatterned control and that patterning endothelial cells in this way may allow control over vessel size *in vivo*. These results represent a step forward towards replicating the hierarchy of natural vascular networks in permissive host settings *in vivo*, as guided vascularization led to the formation of larger vessel “trunks” with lumen diameters of 20-40μm with smaller 5-15μm vessels formed “branches”.

While we had confirmed that guided vascularization can be used successfully for cardiac tissue engineering applications in an appropriate host (athymic mouse), we still had not explained why this technique failed to perform similarly in the athymic rat heart[151]. To answer this question, we directly compared human cardiac tissues with EC cords implanted epicardially in either athymic mice or athymic rats. We found that guided vascularization occurred only in athymic mice, whereas tissues in athymic rats instead exhibited signs of inflammation. Despite this failure of guided vascularization, rats supported larger human cardiac grafts compared to patches implanted in mice, indicating that vascularization and cardiomyocyte engraftment require different host environments. These data suggest that in the future, host factors could potentially be leveraged to improve engraftment of vascular or parenchymal cells such as cardiomyocytes.

Based on the dramatic difference we observed in inflammatory response between these models, we speculated that a heightened innate immune response in the athymic rat heart may promote cardiomyocyte engraftment while interfering with vascularization. Athymic nude mice and athymic nude rats both lack mature T lymphocytes, but retain other immune cell types including macrophages, neutrophils, dendritic cells, NK cells, and B cells. Despite their apparently similar immune systems, differences in immune function between these models has been reported[182,183]. For example, while NK cell activity is elevated in both athymic rodent models, athymic rats have very high NK activity in the peritoneal cavity, whereas athymic mice have relatively low peritoneal NK activity[184]. It is possible that this animal model difference could explain our finding that abdominal cords implants remained intact in the mouse abdomen but were obliterated in the rat. In addition to heightened NK activity, enhanced macrophage activity has been reported in both athymic mice[185] and athymic rats[183]. Mounting evidence points to the critical role of innate immunity in cardiac regenerative medicine[174,186]. In fact, recent groundbreaking work has suggested that the success of cellular therapies in the heart is primarily explained by the macrophage-predominant immune response induced by these therapies[174]. We thus speculate that a heightened innate immune response in athymic nude rats compared to athymic nude mice contributed to superior cardiomyocyte engraftment while interfering with vessel patterning[174].

Taken together, our results suggest that tissue engineering and cellular therapy fields would benefit from paying more careful attention to understanding and tuning host environment to achieve clinical success and ensure reproducibility. A challenge across biomedical research is the widespread replication crisis, which wastes limited resources, erodes public confidence in science, and impedes progress towards clinical translation[187]. Within tissue engineering and regenerative medicine, the neglected role of host biology may contribute to the high rate of pre-clinical failure and irreproducible findings[188]. This is likely particularly important in the pre-clinical development process, as new technologies are typically tested in increasingly larger animal models prior to human clinical trials. We suggest that increased attention to host biology could improve reproducibility and accelerate clinical translation of regenerative therapies, and potentially even be deployed to greatly enhance the efficacy of regenerative engineering strategies.

CHAPTER 5. SUMMARY AND CONCLUSIONS

Engineered tissues could pave the way for new therapies to treat human disease, yet vascularization remains a barrier to the clinical translation of this technology. Without a vascular network to deliver oxygen and nutrients throughout tissues, it is not possible to engineer complex organs such as the heart. Thus, methods for building artificial vessel networks in engineered tissues are required. Importantly, to support tissue function, these artificial networks must be able to rapidly integrate with host circulation *in vivo*. Yet the host factors that control vascular integration in artificial tissues are not well understood. This thesis seeks to address this knowledge gap by exploring host factors that govern vascularization and integration of engineered tissues.

To address the challenge of vascularizing artificial tissues, we must first understand how vascularization occurs in biologic system. In Chapter 1, we review Nature's methods for assembling vascular networks and discuss what is needed to complete our "blueprint" of vascular biology, topology, and function. Following our discussion of vascular biology, in Chapter 2 we present methods that engineers have used to recapitulate the natural features of vascular networks in artificial systems. We compare fabrication methods with varying degrees of top-down control, from self-assembled vascular organoids[9] to recently improved bioprinting methods[80] and highlight the need for hybrid strategies that fuse technology with biology. Later, in Chapters 3 and 4, we use one of these hybrid strategies to study the role of host biology in the vascular integration of engineered tissues. Our method uses technology to pattern endothelial cells and collagen into cord-like structures which then guide biology-driven vessel formation *in vivo*[142]. In the rest of this thesis, we use the EC cords platform to study host factors that affect guided vascularization and integration of artificial cardiac tissues.

In Chapter 3, we report an aberrant response to artificial tissues with EC cords implanted in the athymic rat heart[151]. While previous studies have shown that similar tissues implanted in the mouse abdomen form persistently patterned micro-vessels along each cord[142], we found only transient vessel patterning occurred in the rat heart. Instead, large, blood filled lumens associated with cords at 3 days, but patterning was obliterated at 7 days. Corresponding with this loss of patterning, we also observed markers of increased inflammation characterized by macrophage infiltration and collagen deposition. The increased inflammation and loss of patterning in the rat heart versus what has been reported in the mouse abdomen led us to examine which host factors were driving these differences.

The studies in Chapter 4 compare guided vascularization and tissue integration in constructs implanted across anatomic location and species. We did not find a difference in tissue structure or vascularization between IP and supra-epicardial implants in athymic mice. Instead, guided vascularization led to patterned, perfused vessel formation in both locations. We next compared integration of an artificial cardiac tissue implanted in athymic mice and athymic rats. Cardiac patches implanted in mice displayed patterned graft-derived vessels filled with host blood, indicating that guided vascularization had occurred. Additionally, we found that EC cords more efficiently recruited mouse blood than unpatterned constructs. Whereas implants in rat hearts became inflamed and did not show vessel patterning, we were surprised to observe larger human cardiac grafts in rats compared to mice. To summarize these findings, guided vascularization occurs readily in athymic mice but not athymic rats, while cardiomyocyte engraftment is better supported by the athymic rat host environment. These results led us to conclude that cardiomyocyte engraftment and guided vascularization are regulated by different sets of host factors.

The findings contained in this thesis point to the critical importance of host biology in determining the success of tissue engineering strategies. We are concerned that the challenges we reported in transferring a vascularization strategy between relatively similar rodent species will be amplified as tissue engineering technologies are developed for clinical applications. During the process of pre-clinical and clinical development, technologies must perform in a variety of different species. At a minimum, this typically includes trials in rodents, a large animal model, and eventually human clinal trials. Thus, to prevent costly failures it is important for engineers to understand and adapt to differences between these host environments. Future studies should seek to further investigate the effect of host environment on artificial tissue integration by comparing additional species, strains, and implant locations. Through these studies, it will be necessary to identify specific host factors and underlying biologic mechanisms that regulate aspects of tissue integration including vascularization, inflammation, and parenchymal cell engraftment. Once identified, engineers can develop strategies to optimize these aspects of host biology for the successful integration of artificial tissues.

CHAPTER 6. BIBLIOGRAPHY

1. Ertürk, A. *et al.* Three-dimensional imaging of solvent-cleared organs using 3DISCO. *Nature Protocols* **7**, 1983–1995 (2012).
2. Kirst, C. *et al.* Mapping the Fine-Scale Organization and Plasticity of the Brain Vasculature. *Cell* **180**, 780-795.e25 (2020).
3. Yang, B. *et al.* Single-cell phenotyping within transparent intact tissue through whole-body clearing. *Cell* **158**, 945–958 (2014).
4. Glaser, A. K. *et al.* Multi-immersion open-top light-sheet microscope for high-throughput imaging of cleared tissues. *Nature Communications* **10**, 2781 (2019).
5. Rendeiro, A. F. *et al.* The spatial landscape of lung pathology during COVID-19 progression. *Nature* 1–8 (2021) doi:10.1038/s41586-021-03475-6.
6. Schürch, C. M. *et al.* Coordinated Cellular Neighborhoods Orchestrate Antitumoral Immunity at the Colorectal Cancer Invasive Front. *Cell* **182**, 1341-1359.e19 (2020).
7. Kalucka, J. *et al.* Single-Cell Transcriptome Atlas of Murine Endothelial Cells. *Cell* **180**, 764-779.e20 (2020).
8. Grigoryan, B. *et al.* Multivascular networks and functional intravascular topologies within biocompatible hydrogels. *Science* **364**, 458–464 (2019).
9. Wimmer, R. A. *et al.* Human blood vessel organoids as a model of diabetic vasculopathy. *Nature* **565**, 505–510 (2019).
10. Monteil, V. *et al.* Inhibition of SARS-CoV-2 Infections in Engineered Human Tissues Using Clinical-Grade Soluble Human ACE2. *Cell* **181**, 905-913.e7 (2020).
11. Rayner, S. G. *et al.* Multiphoton-Guided Creation of Complex Organ-Specific Microvasculature. *Advanced Healthcare Materials* 2100031 (2021) doi:https://doi.org/10.1002/adhm.202100031.
12. Monahan-Earley, R., Dvorak, A. M. & Aird, W. C. Evolutionary origins of the blood vascular system and endothelium. *J Thromb Haemost* **11**, 46–66 (2013).
13. Wyatt, S. B. *et al.* Racism and cardiovascular disease in African Americans. *Am J Med Sci* **325**, 315–331 (2003).
14. Zhang, X. *et al.* Racial/ethnic disparities in waitlisting for deceased donor kidney transplantation 1 year after implementation of the new national kidney allocation system. *Am J Transplant* **18**, 1936–1946 (2018).
15. Purnell, T. S. *et al.* Association of Race and Ethnicity With Live Donor Kidney Transplantation in the United States From 1995 to 2014. *JAMA* **319**, 49–61 (2018).
16. Lackland, D. T. Racial Differences in Hypertension: Implications for High Blood Pressure Management. *Am J Med Sci* **348**, 135–138 (2014).
17. Weinberg, C. B. & Bell, E. A blood vessel model constructed from collagen and cultured vascular cells. *Science* **231**, 397–400 (1986).
18. Quint, C. *et al.* Decellularized tissue-engineered blood vessel as an arterial conduit. *Proc Natl Acad Sci U S A* **108**, 9214–9219 (2011).
19. L'Heureux, N. *et al.* Human tissue-engineered blood vessels for adult arterial revascularization. *Nature Medicine* **12**, 361–365 (2006).
20. Dahl, S. L. M. *et al.* Readily available tissue-engineered vascular grafts. *Sci Transl Med* **3**, 68ra9 (2011).

21. Kucukgul, C. *et al.* 3D bioprinting of biomimetic aortic vascular constructs with self-supporting cells. *Biotechnol Bioeng* **112**, 811–821 (2015).
22. Niklason, L. E. & Lawson, J. H. Bioengineered human blood vessels. *Science* **370**, (2020).
23. Song, H.-H. G., Rumma, R. T., Ozaki, C. K., Edelman, E. R. & Chen, C. S. Vascular Tissue Engineering: Progress, Challenges, and Clinical Promise. *Cell Stem Cell* **22**, 340–354 (2018).
24. Kubota, Y., Kleinman, H. K., Martin, G. R. & Lawley, T. J. Role of laminin and basement membrane in the morphological differentiation of human endothelial cells into capillary-like structures. *J Cell Biol* **107**, 1589–1598 (1988).
25. Koike, N. *et al.* Creation of long-lasting blood vessels. *Nature* **428**, 138–139 (2004).
26. Levenberg, S. *et al.* Engineering vascularized skeletal muscle tissue. *Nature Biotechnology* **23**, 879–884 (2005).
27. Stevens, K. R. *et al.* Physiological function and transplantation of scaffold-free and vascularized human cardiac muscle tissue. *Proc Natl Acad Sci U S A* **106**, 16568–16573 (2009).
28. Goldie, L. C., Nix, M. K. & Hirschi, K. K. Embryonic vasculogenesis and hematopoietic specification. *Organogenesis* **4**, 257–263 (2008).
29. Drake, C. J. Embryonic and adult vasculogenesis. *Birth Defects Research Part C: Embryo Today: Reviews* **69**, 73–82 (2003).
30. Jain, R. K. Molecular regulation of vessel maturation. *Nature Medicine* **9**, 685–693 (2003).
31. Carmeliet, P. & Jain, R. K. Molecular mechanisms and clinical applications of angiogenesis. *Nature* **473**, 298–307 (2011).
32. Garcia, M. D. & Larina, I. V. Vascular development and hemodynamic force in the mouse yolk sac. *Front. Physiol.* **5**, (2014).
33. Jones, E. A. V., le Noble, F. & Eichmann, A. What determines blood vessel structure? Genetic prespecification vs. hemodynamics. *Physiology (Bethesda)* **21**, 388–395 (2006).
34. Swift Matthew R. & Weinstein Brant M. Arterial–Venous Specification During Development. *Circulation Research* **104**, 576–588 (2009).
35. Folkman, J. & Sing, Y. Angiogenesis. *Journal of Biological Chemistry* **267**, 10931–10934 (1992).
36. Asahara, T. & Kawamoto, A. Endothelial progenitor cells for postnatal vasculogenesis. *American Journal of Physiology-Cell Physiology* **287**, C572–C579 (2004).
37. Brem, H. & Tomic-Canic, M. Cellular and molecular basis of wound healing in diabetes. *J Clin Invest* **117**, 1219–1222 (2007).
38. Gallagher, K. A. *et al.* Diabetic impairments in NO-mediated endothelial progenitor cell mobilization and homing are reversed by hyperoxia and SDF-1α. *J Clin Invest* **117**, 1249–1259 (2007).
39. Takahashi, T. *et al.* Ischemia- and cytokine-induced mobilization of bone marrow-derived endothelial progenitor cells for neovascularization. *Nat Med* **5**, 434–438 (1999).
40. Dome, B. *et al.* Identification and Clinical Significance of Circulating Endothelial Progenitor Cells in Human Non–Small Cell Lung Cancer. *Cancer Res* **66**, 7341–7347 (2006).
41. Tonnesen, M. G., Feng, X. & Clark, R. A. Angiogenesis in wound healing. *J Investig Dermatol Symp Proc* **5**, 40–46 (2000).
42. Fantin, A. *et al.* Tissue macrophages act as cellular chaperones for vascular anastomosis downstream of VEGF-mediated endothelial tip cell induction. *Blood* **116**, 829–840 (2010).

43. Leid Jamison *et al.* Primitive Embryonic Macrophages are Required for Coronary Development and Maturation. *Circulation Research* **118**, 1498–1511 (2016).
44. Gurevich, D. B. *et al.* Live imaging of wound angiogenesis reveals macrophage orchestrated vessel sprouting and regression. *The EMBO Journal* **37**, e97786 (2018).
45. Lin, E. Y. & Pollard, J. W. Tumor-Associated Macrophages Press the Angiogenic Switch in Breast Cancer. *Cancer Res* **67**, 5064–5066 (2007).
46. Lin, E. Y. *et al.* Macrophages Regulate the Angiogenic Switch in a Mouse Model of Breast Cancer. *Cancer Res* **66**, 11238–11246 (2006).
47. Noy, R. & Pollard, J. W. Tumor-Associated Macrophages: From Mechanisms to Therapy. *Immunity* **41**, 49–61 (2014).
48. Tucker, W. D., Arora, Y. & Mahajan, K. Anatomy, Blood Vessels. in *StatPearls* (StatPearls Publishing, 2021).
49. Moini, J. Chapter 5: Anatomy and Physiology of the Cardiovascular System. in *Anatomy and Physiology for Health Professionals* 36–48 (Jones & Bartlett, 2020).
50. Aird William C. Phenotypic Heterogeneity of the Endothelium. *Circulation Research* **100**, 158–173 (2007).
51. Rafii, S., Butler, J. M. & Ding, B.-S. Angiocrine functions of organ-specific endothelial cells. *Nature* **529**, 316–325 (2016).
52. Danese, S., Dejana, E. & Fiocchi, C. Immune Regulation by Microvascular Endothelial Cells: Directing Innate and Adaptive Immunity, Coagulation, and Inflammation. *The Journal of Immunology* **178**, 6017–6022 (2007).
53. Marcu, R. *et al.* Human Organ-Specific Endothelial Cell Heterogeneity. *iScience* **4**, 20–35 (2018).
54. Gunawardana, H. *et al.* Tissue-specific endothelial cell heterogeneity contributes to unequal inflammatory responses. *Scientific Reports* **11**, 1949 (2021).
55. Ferland-McCollough, D., Slater, S., Richard, J., Reni, C. & Mangialardi, G. Pericytes, an overlooked player in vascular pathobiology. *Pharmacology & Therapeutics* **171**, 30–42 (2017).
56. Florey. The endothelial cell. *Br Med J* **2**, 487–490 (1966).
57. Chung, K. *et al.* Structural and molecular interrogation of intact biological systems. *Nature* **497**, 332–337 (2013).
58. Chen, F., Tillberg, P. W. & Boyden, E. S. Expansion microscopy. *Science* **347**, 543–548 (2015).
59. Chen, B.-C. *et al.* Lattice light-sheet microscopy: Imaging molecules to embryos at high spatiotemporal resolution. *Science* **346**, (2014).
60. Asp, M. *et al.* A Spatiotemporal Organ-Wide Gene Expression and Cell Atlas of the Developing Human Heart. *Cell* **179**, 1647-1660.e19 (2019).
61. Eng, C.-H. L. *et al.* Transcriptome-scale super-resolved imaging in tissues by RNA seqFISH+. *Nature* **568**, 235–239 (2019).
62. Moffitt, J. R. & Zhuang, X. Chapter One - RNA Imaging with Multiplexed Error-Robust Fluorescence In Situ Hybridization (MERFISH). in *Methods in Enzymology* (eds. Filonov, G. S. & Jaffrey, S. R.) vol. 572 1–49 (Academic Press, 2016).
63. Junker, J. P. *et al.* Genome-wide RNA Tomography in the Zebrafish Embryo. *Cell* **159**, 662–675 (2014).
64. Wang, X. *et al.* Three-dimensional intact-tissue sequencing of single-cell transcriptional states. *Science* **361**, (2018).

65. Raghavan, S., Nelson, C. M., Baranski, J. D., Lim, E. & Chen, C. S. Geometrically Controlled Endothelial Tubulogenesis in Micropatterned Gels. *Tissue Eng Part A* **16**, 2255–2263 (2010).
66. Chrobak, K. M., Potter, D. R. & Tien, J. Formation of perfused, functional microvascular tubes in vitro. *Microvascular Research* **71**, 185–196 (2006).
67. Bhatia, S. N. & Ingber, D. E. Microfluidic organs-on-chips. *Nature Biotechnology* **32**, 760–772 (2014).
68. Kim, S., Lee, H., Chung, M. & Jeon, N. L. Engineering of functional, perfusable 3D microvascular networks on a chip. *Lab Chip* **13**, 1489–1500 (2013).
69. Zheng, Y. *et al.* In vitro microvessels for the study of angiogenesis and thrombosis. *PNAS* **109**, 9342–9347 (2012).
70. Redd, M. A. *et al.* Patterned human microvascular grafts enable rapid vascularization and increase perfusion in infarcted rat hearts. *Nature Communications* **10**, 584 (2019).
71. Liu, V. A. & Bhatia, S. N. Three-Dimensional Photopatterning of Hydrogels Containing Living Cells. *Biomedical Microdevices* **4**, 257–266 (2002).
72. Zhang, B. *et al.* Biodegradable scaffold with built-in vasculature for organ-on-a-chip engineering and direct surgical anastomosis. *Nat Mater* **15**, 669–678 (2016).
73. Kloxin, A. M., Kasko, A. M., Salinas, C. N. & Anseth, K. S. Photodegradable hydrogels for dynamic tuning of physical and chemical properties. *Science* **324**, 59–63 (2009).
74. Arakawa, C. K., Badeau, B. A., Zheng, Y. & DeForest, C. A. Multicellular Vascularized Engineered Tissues through User-Programmable Biomaterial Photodegradation. *Advanced Materials* **29**, 1703156 (2017).
75. Miller, J. S. *et al.* Rapid casting of patterned vascular networks for perfusable engineered three-dimensional tissues. *Nature Materials* **11**, 768–774 (2012).
76. Kolesky, D. B., Homan, K. A., Skylar-Scott, M. A. & Lewis, J. A. Three-dimensional bioprinting of thick vascularized tissues. *PNAS* **113**, 3179–3184 (2016).
77. Kolesky, D. B. *et al.* 3D Bioprinting of Vascularized, Heterogeneous Cell-Laden Tissue Constructs. *Advanced Materials* **26**, 3124–3130 (2014).
78. Skylar-Scott, M. A. *et al.* Biomanufacturing of organ-specific tissues with high cellular density and embedded vascular channels. *Science Advances* **5**, eaaw2459 (2019).
79. Corbett, D. C., Olszewski, E. & Stevens, K. A FRESH Take on Resolution in 3D Bioprinting. *Trends Biotechnol* **37**, 1153–1155 (2019).
80. Dasgupta, Q. & Black, L. D. A FRESH SLATE for 3D bioprinting. *Science* **365**, 446–447 (2019).
81. Kang, H.-W. *et al.* A 3D bioprinting system to produce human-scale tissue constructs with structural integrity. *Nature Biotechnology* **34**, 312–319 (2016).
82. Pati, F. *et al.* Printing three-dimensional tissue analogues with decellularized extracellular matrix bioink. *Nature Communications* **5**, 3935 (2014).
83. Lee, V. K. *et al.* Generation of Multi-Scale Vascular Network System within 3D Hydrogel using 3D Bio-Printing Technology. *Cell Mol Bioeng* **7**, 460–472 (2014).
84. Lee, A. *et al.* 3D bioprinting of collagen to rebuild components of the human heart. *Science* **365**, 482–487 (2019).
85. Lin, H. *et al.* Application of visible light-based projection stereolithography for live cell-scaffold fabrication with designed architecture. *Biomaterials* **34**, 331–339 (2013).
86. Tsang, V. L. *et al.* Fabrication of 3D hepatic tissues by additive photopatterning of cellular hydrogels. *The FASEB Journal* **21**, 790–801 (2007).

87. Ochs, M. *et al.* The Number of Alveoli in the Human Lung. *Am J Respir Crit Care Med* **169**, 120–124 (2004).
88. Zheng, Y. *et al.* In vitro microvessels for the study of angiogenesis and thrombosis. *PNAS* **109**, 9342–9347 (2012).
89. Bellis, S. L. Advantages of RGD peptides for directing cell association with biomaterials. *Biomaterials* **32**, 4205–4210 (2011).
90. Lutolf, M. P. *et al.* Synthetic matrix metalloproteinase-sensitive hydrogels for the conduction of tissue regeneration: Engineering cell-invasion characteristics. *Proc Natl Acad Sci U S A* **100**, 5413–5418 (2003).
91. Badeau, B. A., Comerford, M. P., Arakawa, C. K., Shadish, J. A. & DeForest, C. A. Engineered modular biomaterial logic gates for environmentally triggered therapeutic delivery. *Nat Chem* **10**, 251–258 (2018).
92. Schechner, J. S. *et al.* In vivo formation of complex microvessels lined by human endothelial cells in an immunodeficient mouse. *PNAS* **97**, 9191–9196 (2000).
93. Levenberg, S., Golub, J. S., Amit, M., Itskovitz-Eldor, J. & Langer, R. Endothelial cells derived from human embryonic stem cells. *PNAS* **99**, 4391–4396 (2002).
94. Levenberg, S. *et al.* Engineering vascularized skeletal muscle tissue. *Nature Biotechnology* **23**, 879 (2005).
95. Chen, X. *et al.* Prevascularization of a Fibrin-Based Tissue Construct Accelerates the Formation of Functional Anastomosis with Host Vasculature. *Tissue Eng Part A* **15**, 1363–1371 (2009).
96. Song, H.-H. G. *et al.* Transient Support from Fibroblasts is Sufficient to Drive Functional Vascularization in Engineered Tissues. *Adv Funct Mater* **30**, (2020).
97. Clevers, H. Modeling Development and Disease with Organoids. *Cell* **165**, 1586–1597 (2016).
98. Zhang, S., Wan, Z. & D. Kamm, R. Vascularized organoids on a chip: strategies for engineering organoids with functional vasculature. *Lab on a Chip* **21**, 473–488 (2021).
99. Matsumoto, K., Yoshitomi, H., Rossant, J. & Zaret, K. S. Liver organogenesis promoted by endothelial cells prior to vascular function. *Science* **294**, 559–563 (2001).
100. Azizoglu, D. B. & Cleaver, O. Blood vessel crosstalk during organogenesis – Focus on Pancreas. *Wiley Interdiscip Rev Dev Biol* **5**, 598–617 (2016).
101. Del Moral, P.-M. *et al.* VEGF-A signaling through Flk-1 is a critical facilitator of early embryonic lung epithelial to endothelial crosstalk and branching morphogenesis. *Dev Biol* **290**, 177–188 (2006).
102. Crivellato, E., Nico, B. & Ribatti, D. Contribution of endothelial cells to organogenesis: a modern reappraisal of an old Aristotelian concept. *J Anat* **211**, 415–427 (2007).
103. Takebe, T. *et al.* Vascularized and functional human liver from an iPSC-derived organ bud transplant. *Nature* **499**, 481–484 (2013).
104. Homan, K. A. *et al.* Flow-enhanced vascularization and maturation of kidney organoids in vitro. *Nat Methods* **16**, 255–262 (2019).
105. Takasato, M. *et al.* Kidney organoids from human iPS cells contain multiple lineages and model human nephrogenesis. *Nature* **526**, 564–568 (2015).
106. Mansour, A. A. *et al.* An in vivo model of functional and vascularized human brain organoids. *Nature Biotechnology* **36**, 432–441 (2018).
107. Rosso, F., Giordano, A., Barbarisi, M. & Barbarisi, A. From cell-ECM interactions to tissue engineering. *J Cell Physiol* **199**, 174–180 (2004).

108. Kaur, S., Kaur, I., Rawal, P., Tripathi, D. M. & Vasudevan, A. Non-matrigel scaffolds for organoid cultures. *Cancer Letters* **504**, 58–66 (2021).
109. Wei, Z., Schnellmann, R., Pruitt, H. C. & Gerecht, S. Hydrogel Network Dynamics Regulate Vascular Morphogenesis. *Cell Stem Cell* **27**, 798-812.e6 (2020).
110. White, S. M. *et al.* Longitudinal in vivo imaging to assess blood flow and oxygenation in implantable engineered tissues. *Tissue Eng Part C Methods* **18**, 697–709 (2012).
111. White, S. M. *et al.* Implanted cell-dense prevascularized tissues develop functional vasculature that supports reoxygenation after thrombosis. *Tissue Eng Part A* **20**, 2316–2328 (2014).
112. Murphy, W. L., Peters, M. C., Kohn, D. H. & Mooney, D. J. Sustained release of vascular endothelial growth factor from mineralized poly(lactide-co-glycolide) scaffolds for tissue engineering. *Biomaterials* **21**, 2521–2527 (2000).
113. Patel, Z. S. *et al.* Dual delivery of an angiogenic and an osteogenic growth factor for bone regeneration in a critical size defect model. *Bone* **43**, 931–940 (2008).
114. Richardson, T. P., Peters, M. C., Ennett, A. B. & Mooney, D. J. Polymeric system for dual growth factor delivery. *Nature Biotechnology* **19**, 1029–1034 (2001).
115. Chen, R. R., Silva, E. A., Yuen, W. W. & Mooney, D. J. Spatio-temporal VEGF and PDGF delivery patterns blood vessel formation and maturation. *Pharm Res* **24**, 258–264 (2007).
116. Freeman, I. & Cohen, S. The influence of the sequential delivery of angiogenic factors from affinity-binding alginate scaffolds on vascularization. *Biomaterials* **30**, 2122–2131 (2009).
117. Badeau, B. A. & DeForest, C. A. Programming Stimuli-Responsive Behavior into Biomaterials. *Annu. Rev. Biomed. Eng.* **21**, 241–265 (2019).
118. Moncion, A. *et al.* Controlled release of basic fibroblast growth factor for angiogenesis using acoustically-responsive scaffolds. *Biomaterials* **140**, 26–36 (2017).
119. Dong, X. *et al.* Controlled delivery of basic fibroblast growth factor (bFGF) using acoustic droplet vaporization stimulates endothelial network formation. *Acta Biomater* **97**, 409–419 (2019).
120. O'Neill, H. S. *et al.* A stimuli responsive liposome loaded hydrogel provides flexible on-demand release of therapeutic agents. *Acta Biomater* **48**, 110–119 (2017).
121. Weis, S. M. & Cheresh, D. A. Pathophysiological consequences of VEGF-induced vascular permeability. *Nature* **437**, 497–504 (2005).
122. Matsumoto, R. *et al.* Vascular endothelial growth factor-expressing mesenchymal stem cell transplantation for the treatment of acute myocardial infarction. *Arterioscler Thromb Vasc Biol* **25**, 1168–1173 (2005).
123. Thomas, C. E., Ehrhardt, A. & Kay, M. A. Progress and problems with the use of viral vectors for gene therapy. *Nature Reviews Genetics* **4**, 346–358 (2003).
124. Wu, P. *et al.* Non-viral gene delivery systems for tissue repair and regeneration. *Journal of Translational Medicine* **16**, 29 (2018).
125. Dang, J. M. & Leong, K. W. Natural polymers for gene delivery and tissue engineering. *Advanced Drug Delivery Reviews* **58**, 487–499 (2006).
126. Corbett, D. C. *et al.* Thermofluidic heat exchangers for actuation of transcription in artificial tissues. *Science Advances* **6**, eabb9062 (2020).
127. Hu, W. *et al.* Optogenetics sheds new light on tissue engineering and regenerative medicine. *Biomaterials* **227**, 119546 (2020).
128. Rhodes, J. M. & Simons, M. The extracellular matrix and blood vessel formation: not just a scaffold. *J Cell Mol Med* **11**, 176–205 (2007).

129. Davis George E. & Senger Donald R. Endothelial Extracellular Matrix. *Circulation Research* **97**, 1093–1107 (2005).
130. Saunders, R. L. & Hammer, D. A. Assembly of Human Umbilical Vein Endothelial Cells on Compliant Hydrogels. *Cell Mol Bioeng* **3**, 60–67 (2010).
131. Dickinson, L. E., Rand, D. R., Tsao, J., Eberle, W. & Gerecht, S. Endothelial cell responses to micropillar substrates of varying dimensions and stiffness. *J Biomed Mater Res A* **100**, 1457–1466 (2012).
132. Califano, J. P. & Reinhart-King, C. A. A Balance of Substrate Mechanics and Matrix Chemistry Regulates Endothelial Cell Network Assembly. *Cel. Mol. Bioeng.* **1**, 122 (2008).
133. LaValley, D. J. & Reinhart-King, C. A. Matrix stiffening in the formation of blood vessels. *Advances in Regenerative Biology* **1**, 25247 (2014).
134. Ghajar, C. M. *et al.* The Effect of Matrix Density on the Regulation of 3-D Capillary Morphogenesis. *Biophys J* **94**, 1930–1941 (2008).
135. Mason, B. N., Starchenko, A., Williams, R. M., Bonassar, L. J. & Reinhart-King, C. A. Tuning three-dimensional collagen matrix stiffness independently of collagen concentration modulates endothelial cell behavior. *Acta Biomater* **9**, 4635–4644 (2013).
136. Yamamura, N., Sudo, R., Ikeda, M. & Tanishita, K. Effects of the mechanical properties of collagen gel on the in vitro formation of microvessel networks by endothelial cells. *Tissue Eng* **13**, 1443–1453 (2007).
137. Polacheck, W. J. *et al.* A non-canonical Notch complex regulates adherens junctions and vascular barrier function. *Nature* **552**, 258–262 (2017).
138. Mack, J. J. *et al.* NOTCH1 is a mechanosensor in adult arteries. *Nat Commun* **8**, 1620 (2017).
139. Galie, P. A. *et al.* Fluid shear stress threshold regulates angiogenic sprouting. *Proc Natl Acad Sci U S A* **111**, 7968–7973 (2014).
140. Song, J. W. & Munn, L. L. Fluid forces control endothelial sprouting. *PNAS* **108**, 15342–15347 (2011).
141. Mandrycky, C., Hadland, B. & Zheng, Y. 3D curvature-instructed endothelial flow response and tissue vascularization. *Science Advances* **6**, eabb3629 (2020).
142. Baranski, J. D. *et al.* Geometric control of vascular networks to enhance engineered tissue integration and function. *Proc Natl Acad Sci U S A* **110**, 7586–7591 (2013).
143. Weijts, B. *et al.* Endothelial struts enable the generation of large lumenized blood vessels de novo. *Nature Cell Biology* **23**, 322–329 (2021).
144. Morgan, J. T. *et al.* Integration of basal topographic cues and apical shear stress in vascular endothelial cells. *Biomaterials* **33**, 4126–4135 (2012).
145. Hatano, R. *et al.* Endothelial cells derived from embryonic stem cells respond to cues from topographical surface patterns. *Journal of Biological Engineering* **7**, 18 (2013).
146. Dreier, B. *et al.* Early responses of vascular endothelial cells to topographic cues. *Am J Physiol Cell Physiol* **305**, C290–C298 (2013).
147. Williams Ian M. & Wu Joseph C. Generation of Endothelial Cells From Human Pluripotent Stem Cells. *Arteriosclerosis, Thrombosis, and Vascular Biology* **39**, 1317–1329 (2019).
148. Palikuqi, B. *et al.* Adaptable haemodynamic endothelial cells for organogenesis and tumorigenesis. *Nature* 1–7 (2020) doi:10.1038/s41586-020-2712-z.
149. McDonald, D. M. & Choyke, P. L. Imaging of angiogenesis: from microscope to clinic. *Nature Medicine* **9**, 713–725 (2003).

150. Stevens, K. R. *et al.* In situ expansion of engineered human liver tissue in a mouse model of chronic liver disease. *Science Translational Medicine* **9**, eaah5505 (2017).
151. Brady, E. L. *et al.* Guided vascularization in the rat heart leads to transient vessel patterning. *APL Bioengineering* **4**, 016105 (2020).
152. Abouna, G. M. Organ Shortage Crisis: Problems and Possible Solutions. *Transplantation Proceedings* **40**, 34–38 (2008).
153. Kempf, H., Andree, B. & Zweigerdt, R. Large-scale production of human pluripotent stem cell derived cardiomyocytes. *Adv. Drug Deliv. Rev.* **96**, 18–30 (2016).
154. Chen, V. C. *et al.* Development of a scalable suspension culture for cardiac differentiation from human pluripotent stem cells. *Stem Cell Res* **15**, 365–375 (2015).
155. Jackman, C. P. *et al.* Engineered cardiac tissue patch maintains structural and electrical properties after epicardial implantation. *Biomaterials* **159**, 48–58 (2018).
156. Zhang, D. *et al.* Tissue-engineered cardiac patch for advanced functional maturation of human ESC-derived cardiomyocytes. *Biomaterials* **34**, 5813–5820 (2013).
157. Shadrin, I. Y. *et al.* Cardiopatch platform enables maturation and scale-up of human pluripotent stem cell-derived engineered heart tissues. *Nature Communications* **8**, 1825 (2017).
158. Tiburcy, M. *et al.* Defined Engineered Human Myocardium With Advanced Maturation for Applications in Heart Failure Modeling and Repair. *Circulation* **135**, 1832–1847 (2017).
159. Vunjak-Novakovic, G. *et al.* Challenges in cardiac tissue engineering. *Tissue Eng Part B Rev* **16**, 169–187 (2010).
160. Burridge, P. W. *et al.* Chemically Defined and Small Molecule-Based Generation of Human Cardiomyocytes. *Nat Methods* **11**, 855–860 (2014).
161. Tohyama, S. *et al.* Distinct Metabolic Flow Enables Large-Scale Purification of Mouse and Human Pluripotent Stem Cell-Derived Cardiomyocytes. *Cell Stem Cell* **12**, 127–137 (2013).
162. Li, W., Germain, R. N. & Gerner, M. Y. Multiplex, quantitative cellular analysis in large tissue volumes with clearing-enhanced 3D microscopy (Ce3D). *Proc. Natl. Acad. Sci. U.S.A.* **114**, E7321–E7330 (2017).
163. Qin, W. *et al.* Depth-resolved 3D visualization of coronary microvasculature with optical microangiography. *Phys Med Biol* **61**, 7536–7550 (2016).
164. Song, S., Xu, J., Men, S., Shen, T. T. & Wang, R. K. Robust numerical phase stabilization for long-range swept-source optical coherence tomography. *J Biophotonics* **10**, 1398–1410 (2017).
165. Deegan, A. J. *et al.* Optical coherence tomography angiography of normal skin and inflammatory dermatologic conditions. *Lasers Surg Med* **50**, 183–193 (2018).
166. Wang, R. K., Zhang, Q., Li, Y. & Song, S. Optical coherence tomography angiography-based capillary velocimetry. *J Biomed Opt* **22**, 66008 (2017).
167. Choi, W. J. *et al.* Characterizing relationship between optical microangiography signals and capillary flow using microfluidic channels. *Biomed Opt Express* **7**, 2709–2728 (2016).
168. Berg, S. *et al.* ilastik: interactive machine learning for (bio)image analysis. *Nature Methods* 1–7 (2019) doi:10.1038/s41592-019-0582-9.
169. Goddard, T. D. *et al.* UCSF ChimeraX: Meeting modern challenges in visualization and analysis. *Protein Sci.* **27**, 14–25 (2018).

170. Chen, X., Nadiarynkh, O., Plotnikov, S. & Campagnola, P. J. Second harmonic generation microscopy for quantitative analysis of collagen fibrillar structure. *Nature Protocols* **7**, 654–669 (2012).
171. Maiullari, F. *et al.* A multi-cellular 3D bioprinting approach for vascularized heart tissue engineering based on HUVECs and iPSC-derived cardiomyocytes. *Scientific Reports* **8**, 13532 (2018).
172. Kellar, R. S., Kleinert, L. B. & Williams, S. K. Characterization of angiogenesis and inflammation surrounding ePTFE implanted on the epicardium. *J. Biomed. Mater. Res.* **61**, 226–233 (2002).
173. Luttikhuizen, D. T. *et al.* The correlation between difference in foreign body reaction between implant locations and cytokine and MMP expression. *Biomaterials* **27**, 5763–5770 (2006).
174. Vagnozzi, R. J. *et al.* An acute immune response underlies the benefit of cardiac stem-cell therapy. *Nature* 1–1 (2019) doi:10.1038/s41586-019-1802-2.
175. Simionescu, A., Schulte, J. B., Fercana, G. & Simionescu, D. T. Inflammation in Cardiovascular Tissue Engineering: The Challenge to a Promise: A Minireview. *Int J Inflam* **2011**, (2011).
176. Jain, R. K., Au, P., Tam, J., Duda, D. G. & Fukumura, D. Engineering vascularized tissue. *Nature Biotechnology* **23**, 821–823 (2005).
177. Kaully, T., Kaufman-Francis, K., Lesman, A. & Levenberg, S. Vascularization--the conduit to viable engineered tissues. *Tissue Eng Part B Rev* **15**, 159–169 (2009).
178. Zhang, M. *et al.* Cardiomyocyte Grafting for Cardiac Repair: Graft Cell Death and Anti-Death Strategies. *Journal of Molecular and Cellular Cardiology* **33**, 907–921 (2001).
179. Laflamme, M. A. *et al.* Cardiomyocytes derived from human embryonic stem cells in pro-survival factors enhance function of infarcted rat hearts. *Nat Biotechnol* **25**, 1015–1024 (2007).
180. Schindelin, J. *et al.* Fiji: an open-source platform for biological-image analysis. *Nature Methods* **9**, 676–682 (2012).
181. Hirschi, K. K. & D’Amore, P. A. Pericytes in the microvasculature. *Cardiovascular Research* **32**, 687–698 (1996).
182. Cook, J. L. & Lewis, A. M. Immunological surveillance against DNA-virus-transformed cells: correlations between natural killer cell cytolytic competence and tumor susceptibility of athymic rodents. *Journal of Virology* **61**, 2155–2161 (1987).
183. Jong, W. H. D. *et al.* The athymic nude rat. III. Natural cell-mediated cytotoxicity. *Clin. Immunol. Immunopathol* 163–172 (1980).
184. Rolstad, B. The athymic nude rat: an animal experimental model to reveal novel aspects of innate immune responses? *Immunol Rev* **184**, 136–144 (2001).
185. Cheers, C. & Waller, R. Activated Macrophages in Congenitally Athymic “Nude” Mice and in Lethally Irradiated Mice. *The Journal of Immunology* **115**, 844–847 (1975).
186. Couto, G. de *et al.* Macrophages mediate cardioprotective cellular postconditioning in acute myocardial infarction. *J Clin Invest* **125**, 3147–3162 (2015).
187. Baker, M. 1,500 scientists lift the lid on reproducibility. *Nature News* **533**, 452 (2016).
188. Cossu, G. *et al.* Lancet Commission: Stem cells and regenerative medicine. *The Lancet* **391**, 883–910 (2018).